

# New Constraints on Cosmic Particle Populations at the Galactic Center using X-ray Observations of the Molecular Cloud Sagittarius B2

FIELD ROGERS,<sup>1</sup> SHUO ZHANG,<sup>2</sup> KERSTIN PEREZ,<sup>1</sup> MAÏCA CLAVEL,<sup>3</sup> AND AFURA TAYLOR<sup>1</sup>

<sup>1</sup>*Massachusetts Institute of Technology, 77 Massachusetts Avenue, Cambridge, MA 02139 USA*

<sup>2</sup>*Bard College, 30 Campus Road, Annandale-on-Hudson, NY 12504 USA*

<sup>3</sup>*Univ. Grenoble Alpes, CNRS, IPAG, 38000 Grenoble, France*

Submitted to ApJ

## ABSTRACT

Located  $\sim 100$  pc from the dynamic center of the Milky Way, the molecular cloud Sagittarius B2 (Sgr B2) is the most massive such object in the Galactic Center region. In X-rays, Sgr B2 shows a prominent neutral Fe  $K\alpha$  line at 6.4 keV and continuum emission beyond 10 keV, indicating high-energy, non-thermal processes in the cloud. The Sgr B2 complex is an X-ray reflection nebula whose total emissions have continued to decrease since the year 2001 as it reprocesses what are likely one or more past energetic outbursts from the supermassive black hole Sagittarius A\*. The X-ray reflection model explains the observed time-variability of the Fe  $K\alpha$  and hard X-ray emissions, and it provides a window into the luminous evolutionary history of our nearest supermassive black hole. In light of evidence of elevated cosmic particle populations in the Galactic Center, recent interest has also focused on X-rays from Sgr B2 as a probe of low-energy (sub-GeV) cosmic particles. In contrast to the time-varying X-ray reflection, in this case we can assume that the X-ray flux contribution from interactions of low-energy cosmic particles is constant in time, such that upper limits on low-energy cosmic particle populations may be obtained using the lowest flux levels observed from the cloud. Here, we present the most recent and correspondingly dimmest *NuSTAR* and *XMM-Newton* observations of Sgr B2, from 2018. These reveal small-scale variations within lower density portions of the Sgr B2 complex, including brightening features, yet still enable the best upper limits on X-rays from low-energy cosmic particles in Sgr B2. We also present Fe  $K\alpha$  fluxes from cloud regions of different densities, facilitating comparison with models of ambient low-energy cosmic particle interactions throughout the cloud.

**Keywords:** Sagittarius B2, Molecular Cloud, X-ray Reflection, Cosmic Ray, Galactic Center

## 1. INTRODUCTION

Centered at  $\sim 100$  pc projected distance from the supermassive black hole Sagittarius A\* (Sgr A\*; [Ghez et al. \(2008\)](#)) at the dynamic center of the Galaxy, and  $\sim 8$  kpc from Earth, the molecular cloud (MC) Sagittarius B2 (Sgr B2) is the densest and most massive such object in the Central Molecular Zone (CMZ), a region that extends several 100 pc from Sgr A\* and contains  $\sim 10\%$  of the Galaxy's total molecular material ([Morris & Serabyn 1996](#)). X-ray observations of Sgr B2 have revealed strong Fe  $K\alpha$  line emission at 6.4 keV ([Koyama](#)

[et al. 1996](#); [Murakami et al. 2001](#); [Koyama et al. 2007](#); [Terrier et al. 2010](#); [Inui et al. 2009](#); [Nobukawa et al. 2011](#); [Terrier et al. 2018](#)) as well as a hard continuum up to  $\sim 100$  keV ([Terrier et al. 2010](#); [Revnivtsev et al. 2004](#); [Zhang et al. 2015](#)). These features, which imply energetic, non-thermal interactions capable of ionizing the K-shell electrons of neutral Fe, have made Sgr B2 an object of interest for decades. The X-ray picture is further complicated by the time-varying nature of this emission. Since the peak flux was last observed in 2001, the Fe  $K\alpha$  emission has decreased with every subsequent observation, down to  $\sim 20\%$  of the peak by 2013 ([Zhang et al. 2015](#); [Terrier et al. 2018](#)), and the continuum emission from the complex overall has correspondingly decreased by  $\sim 50\%$  from 2003 to 2019 ([Kuznetsova et al. 2021](#)).

In a simplified model, Sgr B2 consists of a dense  $((3 - 9) \times 10^6 \text{ H}_2 \text{ cm}^{-3})$  star-forming core with radius  $\sim 2 - 4''$ , or  $\sim 0.15 - 0.3 \text{ pc}$  given  $\sim 8 \text{ kpc}$  distance to Sgr B2 (Reid et al. 2009). The core is surrounded by an envelope of intermediate density  $(10^4 - 10^5 \text{ H}_2 \text{ cm}^{-3})$  with radius  $2.2'$ , or  $\sim 5 \text{ pc}$ , and an extended diffuse  $(\sim 10^3 \text{ H}_2 \text{ cm}^{-3})$  region with radius  $\sim 9.9'$  or  $\sim 22.5 \text{ pc}$ . The model reproduces the observed column density  $N_H \sim 10^{24} \text{ cm}^{-2}$  through the core and the total mass  $\sim 6 \times 10^6 M_\odot$  of Sgr B2 (Lis & Goldsmith 1990; de Vicente et al. 1997). In reality, Sgr B2 has a more complicated structure including several subdominant cores (Benson & Johnston 1984; Sato et al. 2000; Etzaluze et al. 2013) and an asymmetric overall gas distribution as revealed by images of cold dust (Molinari et al. 2011).

In the X-ray reflection nebula (XRN) model, the Fe  $K\alpha$  X-rays originate in the reprocessing of external X-rays via K-shell photoionization and subsequent fluorescence of neutral iron gas while the continuum emission arises from inverse Compton scattering in the cloud (Sunyaev et al. 1993; Koyama et al. 1996; Sunyaev & Churazov 1998). Reprocessing of X-rays from past flaring activity from Sgr A\* is the widely accepted explanation of the time-variable Fe  $K\alpha$  emission in Sgr B2. An outburst with luminosity  $L_x \sim 10^{39} \text{ erg s}^{-1}$  several hundred years ago and lasting  $\gtrsim 10$  years (Koyama et al. 1996; Terrier et al. 2010), or, alternatively, a shorter and brighter event taking  $> 10$  years to traverse the cloud, (Terrier et al. 2018) could explain the observed peak luminosity from the Sgr B2 core as well as the subsequent dimming, which is expected as the wavefront of the outburst passes through the cloud (Sunyaev et al. 1993).

Though direct observation shows that Sgr A\* is presently in a quiescent state (Baganoff et al. 2003), the XRN model of Sgr B2 and other MCs in the CMZ reveals that Sgr A\* has been brighter in the past few hundred years, with at least two short outbursts (Clavel et al. 2013; Chuard et al. 2018; Terrier et al. 2018). Possible indication of the brilliance of Sgr A\* in the more distant past, over  $10^6$  years ago, comes from observation of the Fermi Bubbles (Su et al. 2010; Dobler et al. 2010), a  $\sim 15 \text{ kpc}$  bi-lobed  $\gamma$ -ray structure extending out of the Galactic Plane, as well as from the even more extended X-ray eROSITA bubbles (Predehl et al. 2020), the  $\sim 100 \text{ pc}$  X-ray Chimneys (Ponti et al. 2019), and the  $\sim 450 \text{ pc}$  radio lobes (Heywood et al. 2019). The origin of these structures is debated, but may be due to a past Active Galactic Nucleus (AGN) phase of Sgr A\* (reviews in (Yang et al. 2018; Kataoka et al. 2018; Zhang & Guo 2020; Sofue & Kataoka 2021)).

A portion of the X-ray emission from Sgr B2 could instead arise from low-energy ( $< 1 \text{ GeV}$ , i.e. highly ioniz-

ing) cosmic-ray (LECR) electrons or protons, where the Fe  $K\alpha$  line arises from K-shell ionization of neutral iron and the continuum emission arises from Bremsstrahlung processes (Valinia et al. 2000; Dogiel et al. 2009b; Yusef-Zadeh et al. 2007; Tatischeff et al. 2012). Neither can explain the full time-varying flux. The cooling time for  $\sim 100 \text{ MeV}$  protons is longer than the observed timescale of the decrease (Terrier et al. 2010). Meanwhile, cooling of LECR electrons could explain the time variability (Yusef-Zadeh et al. 2013), but the peak X-ray flux cannot be easily explained by LECR electrons alone (Revnivtsev et al. 2004), requiring a highly-tuned model, e.g. higher metallicity in Sgr B2 than surrounding clouds (Yusef-Zadeh et al. 2013). However, any steady-state population of LECRs in the cloud contributes a constant X-ray flux, on top of the time-varying XRN flux.

Evidence for elevated LECR populations in the Galactic Center (GC) region relative to our local galactic environment comes principally from modeling observed hydrogen ionization rates at the GC, which are in excess of local rates by a factor of  $\sim 10$  (Le Petit et al. 2016; Oka et al. 2019; Indriolo & McCall 2012). Heating by LECR electrons consistent with the ionization rates would also naturally explain anomalously warm gas temperatures observed in the CMZ (Yusef-Zadeh et al. 2007).

CRs in a broad energy range have also been invoked to explain non-thermal emissions from the GC at a range of wavelengths. TeV-scale  $\gamma$ -ray emission from the GC MCs and centered on Sgr A\* has been taken as evidence of protons up to a few PeV, where the  $\gamma$ -rays originate in the decay of relativistic  $\pi^0$  mesons produced in collisions of the protons with surrounding material (Aharonian et al. 2006; HESS Collaboration et al. 2016), while Yusef-Zadeh et al. (2007) argue that this emission could arise from inverse Compton scattering of submillimeter radiation (observed in the GC and attributed to dust in MCs) by TeV-scale CR electrons. Meanwhile, non-thermal radio filaments have been interpreted as synchrotron radiation from a population of GeV-scale electrons (Yusef-Zadeh et al. 2013; Zhang et al. 2014; Heywood et al. 2019). Similarly, nonthermal X-ray filaments are evidence of TeV-scale electrons (Zhang et al. 2020).

In addition to non-thermal photons, evidence for CRs at the GC comes from observations that could be explained by pressure from CR-driven winds (Heywood et al. 2019; Nakashima et al. 2019; Ponti et al. 2019; Yusef-Zadeh & Wardle 2019; Ponti et al. 2021). Similar winds could be responsible for the Fermi Bubbles, and could explain the observed blue-shifted atomic hydrogen lines from the CMZ (Oka et al. 2019) and high-velocity clouds moving away from the disk (McClure-Griffiths et al. 2013).

Evidence of elevated CR populations in the vicinity of the CMZ motivates a discussion of particle accelerators in the GC and the role of the GC in the dynamics in the Galaxy at large. Despite decades of discussion (Ptuskin & Khazan 1981), these are not presently emphasized in Galactic CR propagation models. The models (i.e. GALPROP (Strong et al. 2007), DRAGON (Evoli et al. 2017)) currently used to predict fluxes at Earth assume CR acceleration in supernova remnants (SNR) distributed throughout the Galactic disk and largely ignore the GC region. However, recent work shows that a portion of CRs at Earth could be due to extreme processes at the GC (Cheng et al. 2012; Jaupart et al. 2018; Anjos & Catalani 2020).

The origin of CRs in the GC is an open topic of discussion. CR acceleration up to  $\sim 100$  TeV is typically credited to SNR. While there are several SNR within  $1^\circ$  of the GC, it is unclear if they can be responsible for the CRs observed today (LaRosa et al. 2000; Yusef-Zadeh et al. 2007; Jouvin et al. 2020; Ponti et al. 2015). Further, in most SNR models, protons cannot be accelerated up to PeV energies (Hillas 2005), so an additional PeVatron would be required to explain the GC cosmic rays. The high-energy source that created the Fermi bubbles and corresponding structures may have been a PeVatron such as an AGN phase of Sgr A\*.  $\gamma$ -ray evidence supports the Sgr A\* PeVatron hypothesis (HESS Collaboration et al. 2016). Meanwhile Cheng et al. (2012) suggested the Fermi bubbles themselves as accelerators for PeV-scale CRs, while observations from HAWC suggest that star forming clusters (not necessarily in the GC) could be accelerators of protons up to PeV scales (Albert et al. 2021). Other possible GC accelerators include pulsars (Guépin et al. 2018), stellar winds (Cesarsky & Montmerle 1983), and magnetic reconnection (Medina-Torrejón et al. 2021).

Measuring X-ray flux levels enables setting upper limits on ionizing power from LECRs within a given region of Sgr B2, as has been the focus of previous studies (Valinia et al. 2000; Dogiel et al. 2009b,a; Terrier et al. 2010; Tatischeff et al. 2012; Zhang et al. 2015). The flux levels can at best result in upper limits on LECRs in the cloud, due to the time-variable XRN component. Limits on X-ray emission from LECR populations in MCs such as Sgr B2 can probe ambient LECR populations in the CMZ, providing valuable input for such CR models, as many accelerators span wide energy ranges, though the ability of LECRs to traverse dense MCs is highly model dependent. Limits on LECR electrons within MCs can also directly constrain relativistic proton populations in the GC, as proton interactions produce LECR electrons within MCs. The interactions of LECRs with clouds is

**Table 1.** *NuSTAR* and *XMM-Newton* observations of Sgr B2.

Instrument	Observation ID	Start Time (UTC)	Exposure (ks)
<i>XMM-Newton</i>	0112971501	2001-04-01T00:25:11	9.2
<i>XMM-Newton</i>	0203930101	2004-09-04T02:53:45	48.5
<i>XMM-Newton</i>	0694640601	2012-09-06T10:56:15	66.6
<i>XMM-Newton</i>	0802410101	2018-04-02T00:59:38	103.0
<i>NuSTAR</i>	40401001002	2018-04-10T12:01:09	149.2

NOTE—The exposure time reported for *XMM-Newton* observations is the *pn*-equivalent exposure.

of interest in its own right because LECRs impact the local environment inside clouds, which is important for star formation (Morlino & Gabici 2015).

In this paper, we present observations of Sgr B2 obtained in 2018 by *XMM-Newton* and *NuSTAR*. Section 2 details the observations and data preparation. In Section 3 we show the X-ray morphology of Sgr B2 while in Section 4 we present spectral analysis of the central region. In Section 5 we compare the 2018 flux with earlier data to discuss the continued decrease in X-ray reflection since 2001, and in Section 6, we set upper limits on ambient LECR proton and electron populations in different regions of Sgr B2. Finally, in Section 7 we discuss these results in the GC context.

## 2. OBSERVATION AND DATA REDUCTION

Table 1 lists the observations discussed in this work. We present new observations of Sgr B2, taken jointly by the *XMM-Newton* and *NuSTAR* X-ray observatories in 2018. For comparison with the 2018 data, we also use select archival *XMM-Newton* observations of Sgr B2.

### 2.1. *XMM-Newton* Observations

*XMM-Newton* consists of three European Photon Imaging Camera (EPIC) instruments: two Metal Oxide Semiconductor (MOS) arrays and a pn array. These cameras detect X-rays from 0.15 – 15 keV with typical energy resolution of  $\sim 2 - 5\%$  and angular resolution of  $6''$  FWHM (Turner et al. 2001; Strüder et al. 2001).

Analysis was performed using the *XMM-Newton* Extended Source Analysis Software (ESAS; Snowden et al. (2008)) distributed with v.12.0.1 of the *XMM-Newton* Science Analysis Software. We reduced the data using the standard procedure and filtered the event files to exclude intervals affected by soft proton contamination.



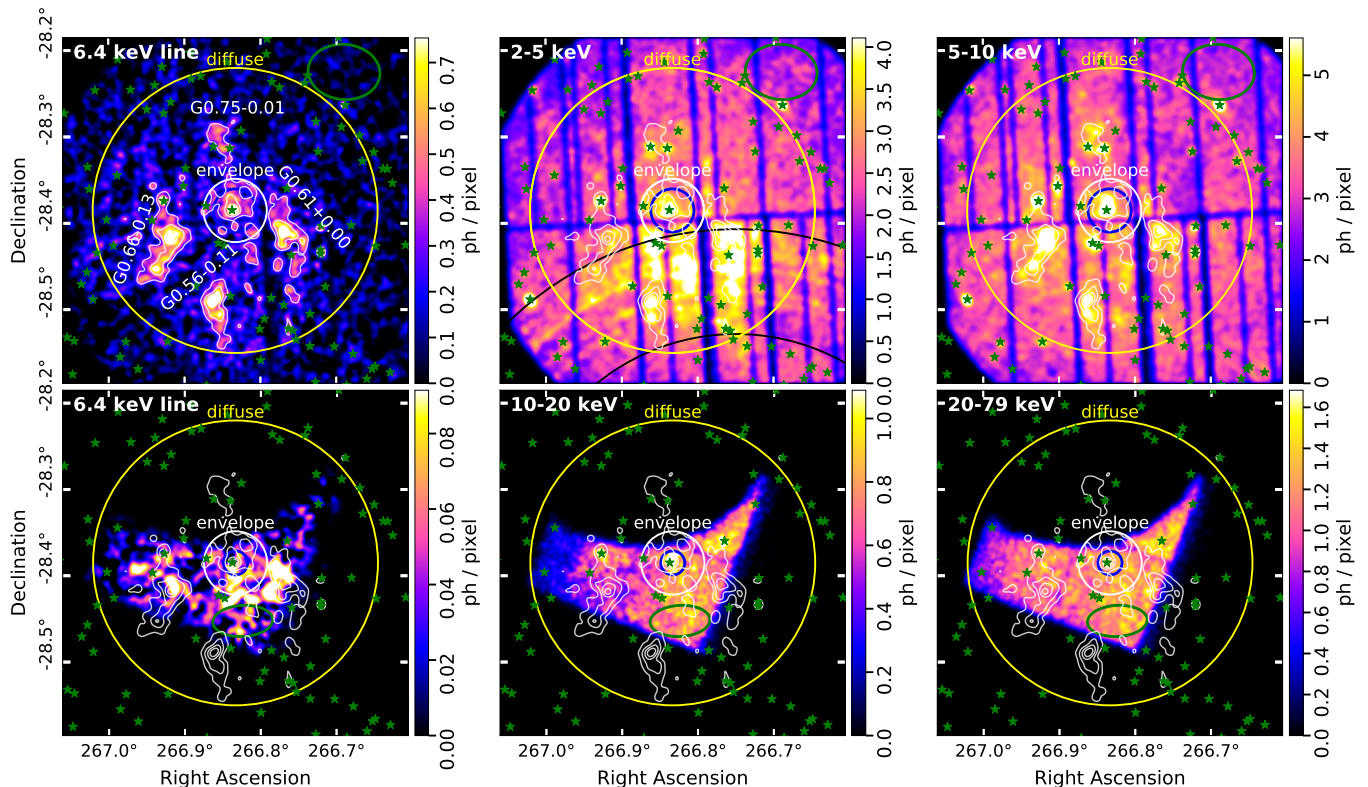


**Figure 1.** The 2018 X-ray morphology of the  $24' \times 24'$  region surrounding Sgr B2 is shown as observed by *XMM-Newton* *pn* (top) in the 6.4 keV line (left), 2 – 5 keV (center), and 5 – 10 keV (right) bands; and by *NuSTAR* *FPMA* (bottom) in the 6.4 keV line (left), 10 – 20 keV (center), and 20 – 79 keV (right) bands. The 6.4 keV line images are continuum subtracted as in Section 3. Contours (white) of the *XMM-Newton* 6.4 keV map are overlaid on all images and illuminate the core and envelope of Sgr B2 as well as several substructures, labelled by their Galactic coordinates. The annular stray light pattern observed in all *EPIC* instruments is most evident in the 2 – 5 keV band (top center, black), while the stray light in *FPMA* is evident the radial region removed from the top-left of the *NuSTAR* images. Circles indicating the diffuse (yellow,  $9.9'$  radius) and envelope (white,  $2.2'$  radius) regions of the simplified model are overlaid, while the core ( $2 - 4''$  radius) is smaller than the angular resolution of both telescopes. The brightest ( $> 10^{-6}$  ph cm $^{-2}$  s $^{-1}$  in 2 – 7 keV) hard X-ray sources from the Chandra Source Catalog 2.0 (Evans et al. 2018) are shown (green stars), as well as the  $90''$  (*XMM-Newton*) and  $50''$  (*NuSTAR*) source regions (blue) and the respective elliptical regions used for background subtraction (green). Color bars indicate intensity in photons per pixel.

Spectra were extracted with the ESAS *mos-spectra* and *pn-spectra* scripts. To account for both internal detector and real sky backgrounds, we chose a local background region for each observation in a sky region without known hard point sources and outside of the spatial extent of Sgr B2. The MOS1 and MOS2 spectra were combined and all were rebinned with  $3\sigma$  significance after background subtraction. We analyzed MOS and *pn* data within the 2–10 and 2–7.8 keV bands, respectively, where the *pn* spectra were truncated due to internal lines around 8 keV.

## 2.2. *NuSTAR* Observations

*NuSTAR* operates in the 3 – 79 keV band using two focal plane modules (*FPMA* and *FPMB*) with angular resolution of  $18''$  (FWHM) and typical energy resolution of 400 eV (FWHM) at 10 keV (Harrison et al. 2013).

The data were reduced and analyzed using the *NuSTAR* Data Analysis Software (*NuSTARDAS*) v.1.3.1 and *HEASOFT* v.6.24. They were filtered for periods of high instrumental background due to South Atlantic Anomaly passages and according to a database of bad detector pixels. In addition, we removed the pixels contaminated by stray light (photons arriving directly onto the detector at large off-axis angles) from bright isolated sources following the model in Krivonos et al. (2014). After removing the contaminated pixels, we were only able to extract spectra from *FPMA*, and only out to a radius of  $50''$ . We used *NuSTAR* spectra in the range of 10 – 20 keV, where the signal-to-noise ratio is highest.

## 3. MORPHOLOGY OF X-RAY EMISSION

Figure 1 presents the 2018 observations in the  $24' \times 24'$  region centered on Sgr B2. The upper panel shows the

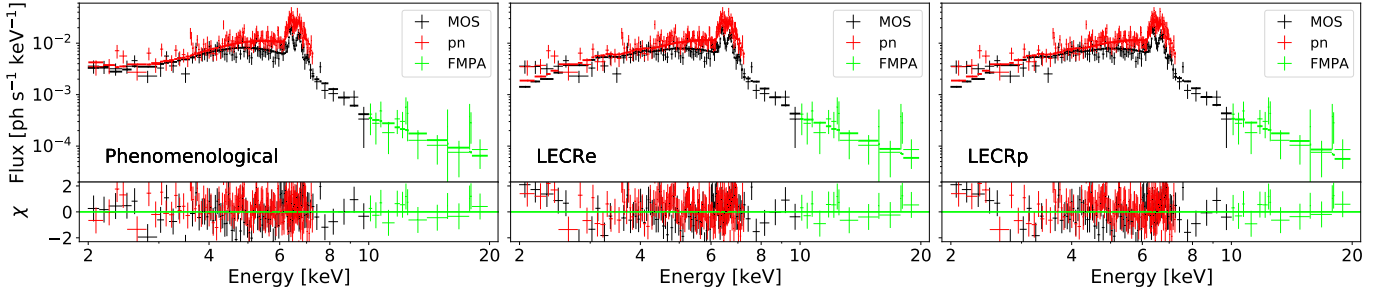


**Figure 2.** The 2018 spectra of the inner 90'' of Sgr B2 as observed by *XMM-Newton* MOS (black, 2 – 10 keV) and *pn* (red, 2 – 7.8 keV) and the inner 50'' as observed by *NuSTAR* FMPA (green, 10 – 20 keV) are fitted with the phenomenological model (left), the LECRe model (center), and the LECRp model (right). The *XMM-Newton* data are binned with  $3\sigma$  confidence level while the *NuSTAR* data are binned with  $1.5\sigma$  confidence level. The best fit is shown in the solid horizontal lines. All three models show satisfactory agreement with the data.

*XMM-Newton* *pn* images in the continuum-subtracted 6.4 keV line and in the 2 – 5 keV and 5 – 10 keV bands. The lower panel presents the *NuSTAR* FMPA images in the continuum-subtracted 6.4 keV line and in the 10 – 20 keV and 20 – 79 keV bands. The 6.4 keV line images were created by subtracting a continuum band, 5.8 – 6.2 keV, from a 6.2 – 6.6 keV signal band. The 90'' (*XMM-Newton*) and 50'' (*NuSTAR*) source regions used for the primary spectral analysis of the core and envelope are shown in dark blue, and the background regions used for spectral analysis with each instrument are in green. The *XMM-Newton* background region is located outside the Sgr B2 complex. In contrast, the *NuSTAR* background region was located within the diffuse region of Sgr B2, due to the limited field of view.

The *XMM-Newton* 6.4 keV line map shows that the core of Sgr B2 is detected at  $13\sigma$  significance within the envelope region. The core is also detected at  $> 5\sigma$  significance in the full energy band of *XMM-Newton* and by *NuSTAR* from 10 – 20 keV. In the 20 – 79 keV band, the *NuSTAR* observation is dominated by background, and the core is not significantly detected ( $< 3\sigma$ ).

In addition to the central core and envelope, Fe K $\alpha$  emission is detected at  $> 5\sigma$  significance from four substructures within the diffuse region of the Sgr B2 in the projected plane. Two of these substructures coincide spatially with the cloud features previously identified by Terrier et al. (2018) as G0.66-0.13 and G0.56-0.11, and G0.66-0.13 was also detected in hard X-rays in the 2013 *NuSTAR* observations (Zhang et al. 2015). Here we additionally report two new substructures, G0.61+0.00 and G0.75-0.01, in the diffuse region of Sgr B2, which were not detected in previous observations. Of these four total substructures, only G0.66-0.13 and G0.61+0.00 lie within the *NuSTAR* field of view. These substructures, which are fainter than the core,

are detected by *NuSTAR* at 6.4 keV but not resolved above background in the higher energy bands.

#### 4. SPECTRAL ANALYSIS OF THE SGR B2 CORE

Figure 2 shows the spectrum of the central region of Sgr B2 as observed in 2018, overlaid with the best fits for several spectral models. In this section, we detail the models, including a phenomenological model in Section 4.1, several models of X-ray reflection in Section 4.2, and the models of LECR-induced X-rays in Section 4.3.

Throughout this section, we extracted spectra from the *XMM-Newton* observations in a 90'' source region, which includes the cloud's core and part of the envelope, consistent with Zhang et al. (2015). Background subtraction was performed using a region outside of Sgr B2, shown in Figure 1. Constrained by stray light contamination, we extracted *NuSTAR* spectra from the inner 50'' and from FMPA only, and due to the smaller field of view of *NuSTAR*, we subtracted a background spectrum extracted from an ellipse located within the diffuse region of Sgr B2, also shown in Figure 1. Background subtraction is expected to account for the instrument background as well a diffuse X-ray emission from the GC region. Any faint point sources within the selected background region are also subtracted. Thus, flux from the diffuse region of Sgr B2 is subtracted from the *NuSTAR* but not *XMM-Newton* spectra, and the spectra have different faint point sources subtracted in this inhomogeneous field. However, above 10 keV, these differences are expected to be small, as hard point sources were not detected in either background region. To compensate for the different source areas and background regions, we used a constant factor to relate the overall flux level from *NuSTAR* to that of *XMM-Newton*. Based on 6.4 keV image analysis of these signal and background regions using *XMM-Newton*, we expect a constant factor

**Table 2.** Best-fit spectral parameters are shown for a joint fit of the 2018 *XMM-Newton* and *NuSTAR* observations, using the central 90'' of Sgr B2 for *XMM-Newton* and central 50'' of Sgr B2 for *NuSTAR*. We report flux parameters for the 90'' region.

Parameter	Unit	Phenomenological <sup>a</sup>	MyTorus <sup>b</sup>	Walls <sup>c</sup>	CREFL16 <sup>d</sup>	LECR <sup>e</sup>	LECRp <sup>e</sup>
$N_H(f)$	$10^{23} \text{ cm}^{-2}$	$0.3 \pm 0.2$	$1.4 \pm 0.1$	$0.9^{+0.1}_{-0.2}$	$1.3 \pm 0.1$	$0.9 \pm 0.1$	$0.9 \pm 0.1$
$N_H(i)$	$10^{23} \text{ cm}^{-2}$	$3.2^{+0.5}_{-0.4}$	$9.0^{+6.0}_{-2.5}$	$7.9^{+3.7}_{-2.1}$	$12.3^{+7.9}_{-4.5}$	$5.2^{+1.2}_{-1.1}$	$5.0^{+0.4}_{-1.0}$
$Z/Z_\odot$ (apec)		2*	2*	2*	2*	2*	2*
$Z/Z_\odot$ (cloud)		...	...	...	1.0*	$1.9^{+0.8}_{-0.4}$	$0.5^{+0.3}_{-...}$
$kT$	keV	$8.6^{+42.0}_{-6.3}$	$6.5^{+0.8}_{-0.7}$	$4.3^{+1.1}_{-0.8}$	$5.4^{+0.6}_{-0.9}$	$4.3^{+1.1}_{-0.7}$	$4.3^{+1.1}_{-0.7}$
$F_{\text{apec}} (2 - 10 \text{ keV})$	$10^{-13} \text{ erg cm}^{-2} \text{ s}^{-1}$	$2.2 \pm 0.2$	$9.5 \pm 0.4$	$5.7 \pm 0.3$	$7.6^{+1.2}_{-0.9}$	$5.6 \pm 0.3$	$5.6 \pm 0.3$
$F_{6.4 \text{ keV}}$	$10^{-6} \text{ ph cm}^{-2} \text{ s}^{-1}$	$6.6 \pm 0.7$	...	...	...	...	...
$\Gamma_{\text{pl}}$		2.0*	...	...	...	...	...
$\theta_{XRN}$		...	...	$28^{+10}_{-16}$	$64^{\circ*}$	...	...
$\Gamma_{XRN}$		...	$2.6 \pm ...$	$1.8^{+0.6}_{-...}$	$2.5^{+...}_{-0.6}$	...	...
$\Lambda$	$10^{24} \text{ H-atoms cm}^{-2}$	...	...	...	...	5.0*	5.0*
$\Gamma_{LECR}$		...	...	...	...	$3.2^{+0.8}_{-0.7}$	$2.9^{+1.6}_{-1.2}$
$E_{\text{min}}$	keV	...	...	...	...	$3.2^{+27.7}_{-2.2}$	$5587^{+54320}_{-5586}$
$N_{LECR}$	$10^{-6} \text{ erg cm}^{-2} \text{ s}^{-1}$	...	...	...	...	$0.9^{+2.0}_{-0.8}$	$0.6^{+75.8}_{-0.5}$
Constant factor		$0.13 \pm 0.04$	$0.19 \pm 0.06$	$0.11^{+0.02}_{-0.03}$	$0.15^{+0.02}_{-0.04}$	$0.12^{+0.06}_{-0.04}$	$0.12^{+0.06}_{-0.04}$
$\chi^2_\nu$ (d.o.f)		0.97 (256)	1.29 (257)	1.09 (256)	1.16 (257)	1.08 (255)	1.08 (255)

NOTE—The goodness of fit is estimated by  $\chi^2_\nu$  and the number of degrees of freedom is given in parentheses. The errors represent 90% confidence. The fluxes and normalizations are for the 90'' region. The constant factor relates the flux from the 50'' *NuSTAR* source region to the 90'' *XMM-Newton* region.

<sup>a</sup>The phenomenological model is given by **wabs\*(apec+wabs\*po+ga+ga+ga)** in **XSPEC**. It is characterized by foreground absorption **wabs**, parametrized by the interstellar hydrogen column density  $N_H(f)$ , and by internal cloud absorption parametrized by column density  $N_H(i)$ . The thermal **apec** component is characterized from metallicity  $Z/Z_\odot$  which could not be constrained and was thus fixed at 2, the plasma temperature  $kT$ , and total flux contribution of  $F_{\text{apec}}$ . The three lines, **ga**, were fixed at 6.4 keV (neutral Fe K $\alpha$ ), 6.7 keV (He-like Fe K $\alpha$ ) and 7.06 keV (neutral Fe K $\beta$ ), and the Fe K $\beta$  flux was fixed at 0.15 of Fe K $\alpha$ . The continuum was modeled by a pure powerlaw **po** characterized by the photon index  $\Gamma_{\text{pl}}$ . We fixed  $\Gamma_{\text{pl}} = 2$  according to the best fit obtained from *NuSTAR* data alone, to avoid skewing by the higher-statistic *XMM-Newton* data.

<sup>b</sup>The MyTorus (Murphy & Yaqoob 2009) model is given by **wabs\*(apec + MYTS + MYTL)** in **XSPEC**, where MYTS and MYTL are two models representing the scattered continuum and fluorescent line emissions, respectively. MyTorus is parameterized by the photon index  $\Gamma$  of the external X-ray population, the internal column density  $N_H(i)$ , and an overall normalization  $N$ , with all parameters coupled between MYTS and MYTL for consistency.

<sup>c</sup>The Walls model is given by **wabs\*(apec+Walls)** in **XSPEC** (Walls et al. 2016), where Walls is parametrized by the photon index  $\Gamma$  of the external X-ray population, the internal column density  $N_H(i)$ , and the inclination angle  $\theta$  of the cloud relative to the X-ray source, as well as an overall normalization factor  $N$ .

<sup>d</sup>The CREFL16 model is given by **wabs\*(apec+CREFL)** in **XSPEC** (Churazov et al. 2017). It is parametrized by metallicity  $Z/Z_\odot$ ,  $\theta$ ,  $\Gamma_{XRN}$ , and  $\tau_T = 2\sigma_T N_H(i)$ , where the Thomson cross section  $\sigma_T = 66.5 \text{ fm}^2$ , as discussed in the text. Here we report  $N_H(i)$  directly for comparison with the other models.

<sup>e</sup>The LECR models are given by **wabs\*(apec+wabs\*LECR)** in **XSPEC**, where LECR is the electron (LECR<sub>e</sub>) or proton (LECR<sub>p</sub>) **XSPEC** model (Tatischeff et al. 2012). The LECR models are characterized by the maximum path length  $\Lambda$  of particles in the cloud, as well as the minimum energy  $E_{\text{min}}$  of particles able to traverse the cloud, and the metallicity  $Z/Z_\odot$  of the cloud. In addition to these cloud parameters, the spectral index  $\Gamma_{LECR}$  of the incident particle population is obtained in the fit.

\*Starred parameters were not allowed to vary in the fit

of  $\sim 0.2$ . In principle, the constant factor could be energy dependent owing to the differences in diffuse emission between the background regions. However, while diffuse emission can be structured on small scales at lower energies, it is more uniform above 10 keV, justifying the use of an energy-independent constant.

In all models discussed below, we use `apec` to model thermal emissions remaining after background subtraction, following Zhang et al. (2015). Other previous works used two `apec` components (Muno et al. 2004; Walls et al. 2016), where the cooler component at 1–2 keV accounts for diffuse GC X-ray emission while the warmer component at 6–8 keV accounts for unresolved point sources. Here, we use a single `apec`, for direct comparison with results in Zhang et al. (2015). There were no significant differences in the non-thermal model parameters between our reported results using the single `apec` model and fits using two `apec` components with fixed temperatures.

In Sections 4.1–4.3 we also consider fitted metallicity  $Z/Z_\odot$  as a metric for the physicality of a fit. In the CMZ, we expect  $Z/Z_\odot$  in the range of 1–2, based on previous measurements (Nobukawa et al. 2011; Revnivtsev et al. 2004; Jones et al. 2011). We assume  $Z/Z_\odot = 2$  but consider  $1 < Z/Z_\odot < 2$  as reasonable.

#### 4.1. Phenomenological Model

Throughout this paper, we use a phenomenological XSPEC model to directly evaluate the 6.4 keV line flux. The phenomenological model is detailed by Zhang et al. (2015) and given by `wabs*(apec+wabs*po+ga+ga+ga)`. The powerlaw continuum (`po`) and the neutral Fe  $K\alpha$  (6.4 keV) and  $K\beta$  (7.06 keV) lines (`ga`) expected in both the X-ray reflection and LECR scenarios are included explicitly. The model also accounts for thermal plasma (`apec`) and ionized Fe  $K\alpha$  (`ga`, 6.7 keV) emissions that persist after background subtraction, as well as both intrinsic and foreground absorption (`wabs`). All spectral fits use the `wabs` model, rather than updated models such as `tbabs`, to facilitate direct comparison with previous works.

We fixed the line energies at 6.4 keV, 6.7 keV, and 7.06 keV and the line widths at 10 eV, i.e. much less than the energy resolution of the instruments. We also fixed the Fe  $K\beta$  normalization at  $K\beta/K\alpha = 0.15$  (Murakami et al. 2001). After obtaining a spectral index  $\Gamma \sim 2$  from a fit to the *NuSTAR* data only, consistent with previous measurements (Terrier et al. 2010; Zhang et al. 2015), we fixed  $\Gamma = 2$  in the combined *NuSTAR* and *XMM-Newton* fit to prevent the higher statistics of the *XMM-Newton* data from skewing  $\Gamma$  away from the best fit at higher energies, where the powerlaw component

dominates. We fitted the `apec` plasma temperature but fixed the `apec` metallicity  $Z/Z_\odot = 2$  because it was not constrained by the data. The intrinsic and foreground hydrogen column densities,  $N_H(i)$  and  $N_H(f)$ , in `wabs`, also varied freely.

Figure 2 (left) shows the spectral fit for the inner 90'', and the best fit model parameters are in Table 2. We obtained a satisfactory fit with  $\chi^2_\nu = 0.97$  for 256 d.o.f. While the best fit foreground column density,  $N_H(f) = 0.3 \pm 0.2 \times 10^{23} \text{ cm}^{-2}$ , was on the low side of the expected value of  $0.7 \times 10^{23} \text{ cm}^{-2}$  to the GC, the fitted intrinsic column density  $N_H(i) = 3.2^{+0.5}_{-0.4} \times 10^{23} \text{ cm}^{-2}$  was low compared to both the best fit of  $6.8 \pm 0.5 \times 10^{23} \text{ cm}^{-2}$  found with INTEGRAL/IBIS (Terrier et al. 2010) and  $5.0 \pm 1.3 \times 10^{23} \text{ cm}^{-2}$  with *NuSTAR* (Zhang et al. 2015). However, we do not expect a physical value for  $N_H(i)$  in this case because it only represents an average over the region, rather than the complex scattering dynamics in the cloud. We note that all non-thermal parameters are consistent between the values reported here and those obtained in a fit with a two-`apec` plasma.

#### 4.2. X-ray Reflection Nebula Models

Several self-consistent XSPEC models of the XRN scenario have been developed. In contrast with the phenomenological model, these models require physical correlation between the fluorescence lines and the continuum emissions. Thus, they can in general be used to understand the primary X-rays whose reflection gave rise to the XRN. Because the X-ray reflection is no longer in its bright state, we cannot use the 2018 data to extract information beyond that obtained by previous analyses about the presumed Sgr A\* flare responsible for this emission (Walls et al. 2016). However, we present the spectral fits and associated parameters for the 2018 observations, because they show that the 2018 spectra are consistent with arising primarily from X-ray reflection.

Previously, Zhang et al. (2015) modeled X-ray reflection from Sgr B2 using the *MyTorus* X-ray Reprocessing Model (Murphy & Yaqoob 2009; Yaqoob 2012), developed for X-ray reflection from toroid structures surrounding Compton-thick AGN. *MyTorus* is parametrized by the cloud hydrogen column density  $N_H(i)$ , the spectral index  $\Gamma$  of the external X-ray source, and an overall normalization. The model is additionally parametrized by an inclination angle of the torus relative to the source, which we fix at  $0^\circ$  to most closely describe the situation of a spherical cloud. *MyTorus* has additional limitations beyond geometry, detailed by Zhang et al. (2015), when applied to model MCs as XRN, and in particular it assumes reflection in a medium with metallicity  $Z = Z_\odot$  and uniform density. *MyTorus* is implemented



as a series of models in XSPEC. To best approximate the MC scenario, we used two MyTorus components, describing the scattered continuum (MYTS) and the iron fluorescence lines (MYTL), with all parameters coupled between these components so that they were consistent with arising from the same incident X-rays. For consistency with Zhang et al. (2015), we used the models with reflected X-rays up to 500 keV and an energy offset of +40 eV for the fluorescent lines. Thus the XSPEC model is `wabs*(apec+MYTS+MYTL)`, where the MyTorus components are `mytorus_scatteredH500_v00.fits` and `mytl_V000010pEp040H500_v00.fits`, and the thermal plasma `apec` parameters are as in Section 4.1. The fit is marginal with  $\chi^2_\nu = 1.29$  for 257 d.o.f. Additionally, both the intrinsic and foreground column densities are fitted much higher than the physical expectation, and the `apec` component absorbed a flux somewhat larger than expected based on the phenomenological model fit, possibly because it was compensating for low compatibility of the myTorus model with the data. Thus, the 2018 data are not well suited for the MyTorus model with physical parameters. However, due to the limitations of the myTorus model in describing Sgr B2, we do not exclude the XRN scenario based on this result.

The Monte Carlo model developed by Walls et al. (2016), hereafter the Walls model, was developed specifically to model MCs as XRN with the particular application of constraining the location of Sgr B2 relative to Sgr A\*. Like MyTorus, Walls depends on intrinsic absorption  $N_H(i)$  of the cloud and spectral index  $\Gamma$  of the external X-ray source. It is additionally parametrized by the angle  $\theta$  of the spherical cloud relative to the external source, such that  $\theta = 0$ , which is unphysical given the non-zero projected distance from Sgr B2 to Sgr A\*, corresponds to the cloud situated in line between the source and the observer, and the true distance from the X-ray source to the cloud is  $\sim 100 \text{ pc} / \sin \theta$ . The position  $\theta$  of the cloud relative to the source strongly impacts the XRN spectrum, as absorption patterns and effective cloud thickness differ dramatically between X-rays reflected to observers at different  $\theta$ . There are several Walls models with varying cloud metallicities and density profiles. We chose the model with  $Z = Z_\odot$  for direct comparison with spectral fitting by Walls et al. (2016) but note that with these data the metallicity does not significantly change the spectrum below 10 keV, apart from the overall normalization of incident X-rays. We used a uniform, rather than Gaussian, cloud density profile, which gave a better fit and was found to be more suitable by Walls et al. (2016). Thus the model is `wabs*(apec+Walls)` where the Walls component is `Walls_et_al_2016_Uniform_1.0.fits`.

The fit was satisfactory, with  $\chi^2_\nu = 1.09$  for 256 d.o.f. We found the best fit  $\theta = 28^{+10}_{-16}$ , significantly lower than the best fit of  $\theta = 64^{+8}_{-7}$  found for the bright state (Walls et al. 2016). However, since these data do not represent X-ray reflection in the bright state, we caution against overinterpretation of the result. The foreground column density was consistent with previous results at  $N_H(f) = 0.9^{+0.1}_{-0.2} \times 10^{23} \text{ cm}^{-2}$ , and the fitted intrinsic column density was on the high side of previous results, at  $N_H(f) = 7.9^{+3.7}_{-2.1} \times 10^{23} \text{ cm}^{-2}$ . While the source XRN spectral index was not constrained, the flux and temperature of the `apec` component were consistent with expectation, and the data are consistent with XRN origin according to the Walls model.

Finally, the uniform Cloud REFlection of 2016, CREFL16, model (Churazov et al. 2017) treats the case of XRN in a uniform spherical cloud using the same geometry as Walls et al. (2016) but with additional fluorescent lines (beyond Fe) and treating metallicity  $Z/Z_\odot$  as a free parameter. In addition to  $Z/Z_\odot$ , the model parameters include the inclination  $\cos \theta$  to the illuminating source, the spectral index  $\Gamma$  of the illuminating source spectrum, and the optical depth of Thomson scattering,  $\tau_T = \sigma_T n_H R$  where  $\sigma_T \sim 66.5 \text{ fm}^2$  is the Thomson scattering cross section,  $n_H$  is the hydrogen density, and  $R$  is the cloud radius, such that  $N_H(i) = 2n_H R = 2\tau_T / \sigma_T$ . In Table 2 we report  $\theta$  and  $N_H(i)$  for direct comparison with other models. Because the CREFL16 fit favored the unphysical result  $\theta = 0$ , we fixed  $\theta = 64^\circ$  as in Walls et al. (2016). Because the best fit gave  $Z/Z_\odot < 1$ , which is unphysical, we froze the metallicity at solar abundance, the lowest abundance consistent with observation. The fit was acceptable with  $\chi^2_\nu = 1.16$  for 257 dof., but the `apec` component absorbed an order of magnitude more flux than expected, suggesting as with Walls that the CREFL16 model is not best suited for these data. Meanwhile, the `apec` and absorption parameters were consistent with those in the Walls fit.

For all three self-consistent XRN models,  $\chi^2_\nu$  was acceptable, but most model parameters were poorly constrained. In the CREFL16 model, the best fit angle to Sgr B2 was  $\theta = 0$ , but the fit was still acceptable with the constraint  $\theta = 64^\circ$ . While  $\theta = 0$  does not reflect the position of Sgr B2, the preference for  $\theta = 0$  may reflect a situation in which X-rays observed from Sgr B2 in 2018 are produced after the external X-ray front has partially or fully passed through the cloud. In this case, the external X-rays still being reflected have already traversed a cloud depth larger than the typical reflection depth in the bright state, and the effects of multiple scattering may also become important. The fits in this section illustrate that the 2018 flux from the core of Sgr B2 can be



described by the XRN spectral models. However, even if X-ray reflection dominates the 2018 flux, the XRN models do not account for time-dependent effects as the external front passes through the cloud, so we cannot use these results to constrain the external X-ray spectrum.

#### 4.3. Low-energy Cosmic Ray Models

In the assumption that the X-ray emission is now dominated by LECR illumination, we used the **LECR**e and **LECR**p XSPEC models (Tatischeff et al. 2012) to understand if our data is consistent with a LECR-dominated flux and to constrain the possible LECR populations. The XSPEC model was given by **wabs\*(apec+wabs\*LECR)**, where the **wabs** and **apec** components account for foreground and internal absorption and any non-subtracted plasma emissions, treated as in Section 4.1. The LECR models (**LECR**e or **LECR**p) assume a MC is bombarded by CRs from an external source whose spectrum follows a powerlaw with index  $\Gamma_{LECR}$ . The remaining model parameters, including the path length  $\Lambda$  of CRs in the X-ray production (non-thermal) region of the cloud, the minimum energy  $E_{min}$  for a CR to enter the X-ray production region of the cloud, and the metallicity  $Z$ , are properties of the MC. The normalization  $N_{LECR}$  describes the injected power of the cosmic rays from  $E_{min}$  to 1 GeV, with the power  $P_{LECR} = 4\pi D^2 N_{LECR}$  from a surface, given distance  $D$  to the cloud.

The fitted parameters for the **LECR**e and **LECR**p models are in Table 2 and fitted spectra are in Figure 2.  $\Lambda$  could not be constrained by the fits and was frozen at  $5 \times 10^{24}$  H-atoms per  $\text{cm}^2$  in accordance with the column density through the core of Sgr B2. The metallicity in the LECR model is the metallicity of the cloud, which is distinct from that of the **apec** component.

In the electron (**LECR**e) case, the fit for the inner  $90''$  region was satisfactory with  $\chi^2_\nu = 1.08$  for 255 d.o.f. The best-fit foreground  $N_H(f) = (0.9 \pm 0.1) \times 10^{23} \text{ cm}^{-2}$  and intrinsic  $N_H(i) = 5.2^{+1.2}_{-1.1} \times 10^{23} \text{ cm}^{-2}$  are consistent with previous observations. The plasma temperature was  $kT = 4.3^{+1.1}_{-0.7} \text{ keV}$ , and the cloud metallicity was found to be  $Z = 1.9^{+0.8}_{-0.4} Z_\odot$ , consistent with the expected range of  $1 - 2 Z_\odot$ . The fit favored no lower cutoff on CR energies in the cloud, with  $E_{min} = 3.2^{+27.7}_{-2.2} \text{ keV}$ , and an electron spectral index of  $\Gamma_{LECR} = 3.2^{+0.8}_{-0.7}$ . The fit normalization  $N_{LECR} = 0.9^{+2.0}_{-0.8} \times 10^{-6} \text{ erg cm}^{-2} \text{ s}^{-1}$ , for an upper limit (90% confidence) on  $P_{LECR} < 2.2 \times 10^{40} \text{ erg s}^{-1}$  from the core given a distance of  $\sim 8 \text{ kpc}$  to Sgr B2.

In the proton (**LECR**p) case, the fit statistic for the central  $90''$  was also satisfactory, with  $\chi^2_\nu = 1.08$  for 255 d.o.f. The best-fit foreground  $N_H(f) = (0.9 \pm 0.1) \times 10^{23} \text{ cm}^{-2}$  and intrinsic  $N_H(i) = 5.0^{+0.4}_{-1.0} \times 10^{23} \text{ cm}^{-2}$  are

consistent with previous observations. The plasma temperature was  $kT = 4.3^{+1.1}_{-0.7} \text{ keV}$ .  $E_{min}$  was completely unconstrained, while the fit favored a similar CR spectrum as in the **LECR**e case,  $\Gamma_{LECR} = 2.9^{+1.6}_{-1.2}$ . The cloud metallicity was fitted as  $Z < 0.8 Z_\odot$  (90% confidence), which is inconsistent with the expected value of  $1 - 2 Z_\odot$ , so this fit cannot represent a physical scenario, and we cannot set an upper limit on proton populations. However, we can constrain the metallicity at  $Z/Z_\odot = 1$  and obtain a similar quality fit with  $\chi^2_\nu = 1.11$  for 256 d.o.f. In this case, we obtain  $N_{LECR} = 1.7^{+0.5}_{-0.2} \times 10^{-7} \text{ erg cm}^{-2} \text{ s}^{-1}$ , for an upper limit  $P_{LECR} < 1.7 \times 10^{39} \text{ erg s}^{-1}$ .

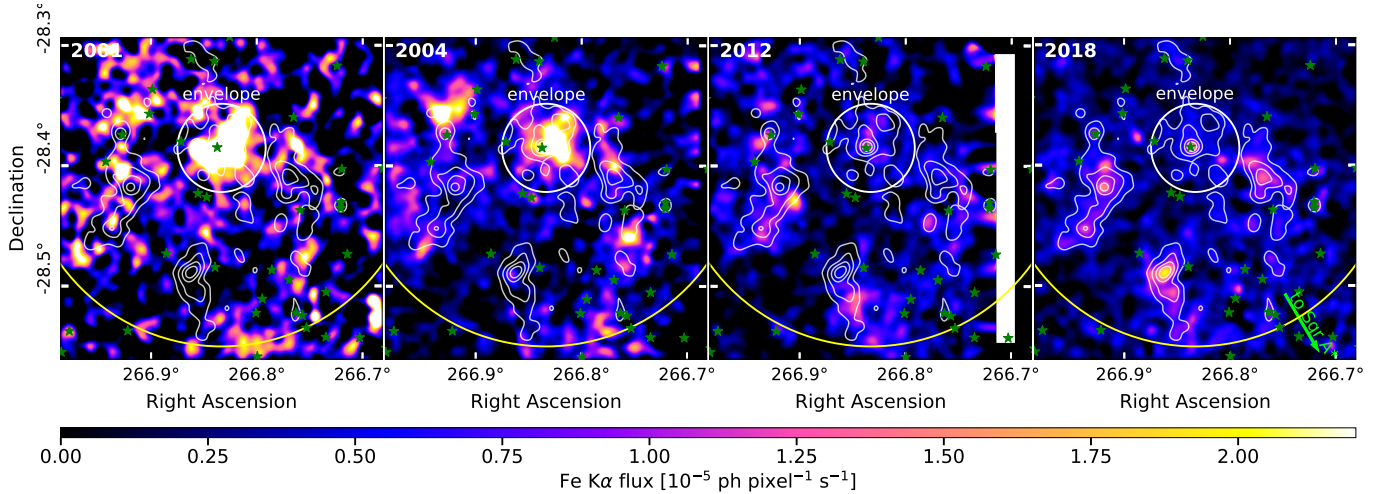
### 5. TIME VARIABILITY OF X-RAY REFLECTION

Figure 3 shows the morphology of 6.4 keV emission in four *XMM-Newton* observations of Sgr B2 from 2001 to 2018. The contour lines of the 2018 6.4 keV emission are overlaid, for comparison with Figure 1 despite the change in color scale. In these exposure-corrected and continuum-subtracted images, the surface brightness of the core and envelope decreases over time. In contrast to the behavior of the core and envelope, bright substructures within the diffuse region, including those identified in Section 3, brighten and dim from one observation to the next. Here, we discuss this changing Fe  $K\alpha$  brightness and morphology from the cloud overall (Section 5.1) and from the substructures (Section 5.2).

#### 5.1. Time Variability of the Central Region

Figure 4 presents light curves of the Fe  $K\alpha$  line flux from Sgr B2, illustrating the behavior of the diffuse, envelope, and core regions. We use a  $6'$  region, which includes the Sgr B2 envelope and core and the bulk of the diffuse portion of the cloud, to illustrate the behavior of the cloud over all. The resulting light curve illustrates that the total flux from Sgr B2 has continued to decrease with time, by a factor of  $\sim 4$  since 2001 and of  $\sim 2.5$  since 2004. This indicates that the bulk of all emissions from the Sgr B2 complex in 2012 and prior are due to X-ray reflection. The  $6'$  region was chosen to directly correspond to the region detected with the INTEGRAL observatory (which has a  $6'$  resolution), facilitating comparison with the light curve of hard continuum emission in Kuznetsova et al. (2021). The observed decrease in Fe  $K\alpha$  emission since 2004 is consistent with the decrease in higher-energy X-rays from INTEGRAL (Kuznetsova et al. 2021), indicating that the two energy scales are linked.

The light curve from the central  $90''$  consists of the Fe  $K\alpha$  line flux measurement from Section 4.1, alongside previous measurements (2001 – 2013) from Zhang et al.



**Figure 3.** The morphology of Fe K $\alpha$  emission from Sgr B2 is shown as observed in 2001 (left), 2004 (center left), 2012 (center right), and 2018 (right) by *XMM-Newton* *pn*. The images are exposure corrected, with continuum subtraction performed as in Figure 1. The contours (white) from Figure 1 illustrate the non-exposure-corrected Fe K $\alpha$  morphology observed in 2018. The modeled diffuse (yellow, 9.9') and envelope (white, 2.2') regions of Sgr B2, as well as the brightest hard X-ray sources (green stars) from the Chandra Source Catalog 2.0 (Evans et al. 2018), are also shown. The arrow (lime) points toward Sgr A\*.

(2015). The data from Zhang et al. (2015) illustrate the compatibility of this work with previous measurements. Consistent with the images in Figure 3, spectral analysis shows that the Fe K $\alpha$  line flux from the central 90'' (core and bulk of the envelope) decreased with each subsequent observation during this time period, by a factor of  $\sim 2$  since 2012, with an overall decrease by a factor of  $\sim 10$  since the peak (2001 and prior). This indicates that, as with the cloud overall, the bulk of emissions from the Sgr B2 core and envelope in 2013 and prior are due to X-ray reflection rather than LECR interactions. We note that the decrease in emissions from the core and envelope is steeper than that from the 6' region.

Finally, we show the light curve for the central 10''-radius region, which corresponds to the  $\sim 15''$  half-power diameter of *XMM-Newton* together with the width of the core. Though the statistics are less significant due to the small size of this region, we observe a similar pattern of decreasing emission after 2004 for the core as for the cloud overall.

We fitted the 90'' light curve as an exponential decrease with a constant offset, as expected from the XRN model as a wavefront passes through a cloud (Sunyaev et al. 1993). We note that the fitted constant offset is poorly constrained, consistent both with 0 and with the 2018 flux level. Further, as shown in Section 4, the spectral analysis of the 2018 observations is consistent with either an entirely XRN or entirely CR origin. Thus we cannot determine if the flux from this central region has reached a constant level or if it will continue to decrease, and hence we only discuss upper limits on LECRs.

In context of the continued flux decrease, Figure 3 illustrates how the geometry of the emission from the core and envelope has changed over time. While the envelope in 2001 was brightest on the Sgr A\* side of the envelope, it was more balanced by 2004, and by 2012 and 2018, the envelope emission was more extensive on the opposite side of Sgr A\*, as illustrated by the contour lines. This provides further indication that the initial flare from Sgr A\* has already passed through some or all of the envelope.

### 5.2. Time Variability of Diffuse Substructures

Figure 5 (panel 1) shows the ellipsoid regions (detailed in Appendix A Table 4) defined to correspond to the substructures identified in Section 3.

The remaining panels in Figure 5 show light curves of 6.4 keV line emission from three of the substructures (G0.66-0.13, G0.56-0.11, and G0.61+0.00) that were significantly detected in 2018. These light curves were produced through spectral fitting of *XMM-Newton* data only, detailed in Appendix A. The substructures behave differently over time, as G0.66-0.13 (black, second panel) brightens in 2012 and then dims again, while G0.56-0.11 (black, third panel) continues to brighten after 2004.

Within each substructure, we defined several 40''-radius circular regions ( $\sim 10$ -year light-crossing time) to illustrate the patterns of light that appear to be moving through the larger substructure. In each substructure, the circles are ordered from least negative declination (A, magenta, i.e. farthest from Sgr A\* in the projected plane) to most negative, and the circle A brightens last.

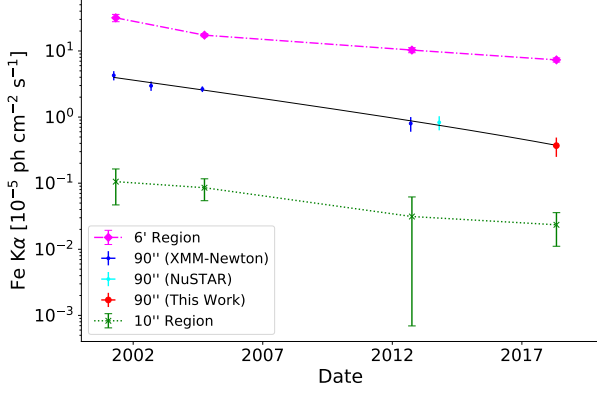


**Figure 4.** Time variability of the neutral Fe K $\alpha$  line flux is shown for a 6'-radius region representing the cloud overall (magenta), the central 90'' (red, blue, and cyan) and the core (red). The light curve of the 6' region, which includes most of the diffuse emission, shows that the Fe K $\alpha$  flux from the cloud overall has decreased to  $23 \pm 4\%$  of the 2001 over this time period. The light curve for the central 90'' contains the data point calculated in Section 4 (red) alongside earlier measurements by Zhang et al. (2015) with *XMM-Newton* (blue), and *NuSTAR* (cyan). The black curve is an exponential fitted to the data. We note that the emissions from the central 90'' fall off more steeply compared to the 6' region, likely due to the effects of the irregularly brightening substructures in the diffuse region. The 2018 Fe K $\alpha$  flux from the inner 90'' of Sgr B2 is  $9 \pm 3\%$  of the value measured in 2001 and  $54 \pm 18\%$  of its value in 2012. The green curve shows the light curve for the central 10''-radius region, which corresponds to the  $\sim 15''$  half-power diameter of *XMM-Newton* together with the width of the core.

For G0.66-0.13, the light curves for circles B and C follow the same pattern as the parent structure, while circle A brightens in 2018, consistent with a flare originating at Sgr A\* propagating through the cloud. We note that while these X-ray substructures were identified within the projected area of diffuse region of Sgr B2, we cannot exclude that they may correspond to other structures along the line of sight but outside of the Sgr B2 complex. Efforts to clarify the location of the substructures using line-of-sight velocity maps from the MOPRA 3 mm survey (Barnes et al. 2015) were inconclusive.

## 6. LOW-ENERGY COSMIC RAY LIMITS

Though cosmic rays cannot explain the time-varying emissions from Sgr B2 (see Section 1), any LECRs present within the cloud would contribute a constant Fe K $\alpha$  and hard continuum flux. In 2018, the Fe K $\alpha$  flux from the core and envelope of Sgr B2 was the lowest yet observed. Since this indicates that the XRN component is at its lowest level yet, any LECR contribution is a larger portion of the 2018 flux compared to previous ob-

servations. Therefore, using the 2018 observations, we can set the most accurate upper limits on iron fluorescence due to LECR populations within Sgr B2. As discussed in Section 5, we only provide upper limits because the flux is also consistent with being still dominated by a time-varying XRN component, and because multiple scattering could also lead to a temporarily flat light curve (of XRN origin) even after the primary reflected wavefront has passed through the cloud. Using spectral analysis of the inner 90'' of Sgr B2, in Section 4.3 we were able to set upper limits on power from LECR interactions within this region,  $P_{LECR_e} < 2.2 \times 10^{40}$  and  $P_{LECR_p} < 1.7 \times 10^{39} \text{ erg s}^{-1}$ .

In this section, we probe 6.4 keV line emissions from different cloud regions, toward understanding LECR populations within Sgr B2 in the context of both ambient LECRs in the CMZ and LECR production in the cloud. The problem of CR transport into and within MCs is model dependent and has been the subject of several theoretical works with different predictions for the geometry of energy deposition by LECRs, all of which necessarily make simplifying assumptions about the gas distribution and magnetic field structure, for either a generic cloud or Sgr B2 specifically (Dogiel et al. 2015; Morlino & Gabici 2015; Gabici 2013; Owen et al. 2021).

In Figure 6, the Herschel hydrogen column density map (Molinari et al. 2011) illustrates the complex and non-uniform structure of Sgr B2 alongside the boundaries associated with the simplified cloud geometry model (Section 1). To probe models of LECRs traversing the cloud, we have identified several sky regions which are compatible with the diffuse, envelope, and core components of Sgr B2 in both the simplified models and the observed hydrogen column density.

In Table 3, we present the Fe K $\alpha$  flux and surface brightness based on fitting with the phenomenological model for the sky regions in Figure 6. Details of the data and fitting are in Appendix A. The Fe K $\alpha$  surface brightness from the representative diffuse, envelope, and core regions of the cloud are  $3.2 \pm 0.9$ ,  $6.5 \pm 1.4$ , and  $16.9 \pm 4.1 \times 10^{-7} \text{ ph cm}^{-2} \text{ s}^{-1} \text{ arcmin}^{-1}$ , respectively.

## 7. DISCUSSION

Using dedicated *XMM-Newton* and *NuSTAR* observations, we have shown that the decrease in total Fe K $\alpha$  emission from the GC MC Sgr B2, which began after the year 2001, has continued through 2018. Detailed analysis reveals a more complex picture, as several substructures within the diffuse region of the cloud have light curves that differ from the average trend. In this section, we discuss implications for the XRN scenario, ambient LECR populations in the CMZ, and LECR pro-

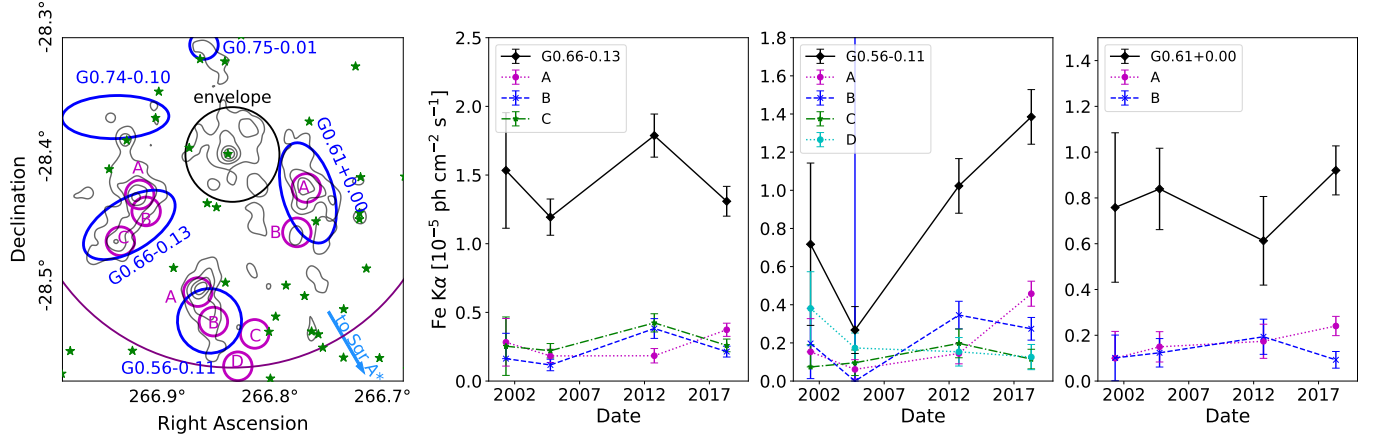


**Figure 5.** *Panel 1:* The contours of the 6.4 keV line emission from 2018 are shown in the same projection as Figure 3. The regions (dark blue) identified as Sgr B2 substructures G0.66-0.13, G0.56-0.11, G0.75-0.10, and G0.61+0.00 are shown. G0.74-0.10, identified by Terrier et al. (2018), is also shown for reference, though it is not detected in 2018 and not treated in this work. We have further identified several 40''-radius features (magenta, A, B, C...) that illustrate the changes in morphology within each substructure over time. All region positions are given in Appendix A Table 4. The arrow (light blue) shows the direction to Sgr A\*. *Panels 2-4:* The remaining panels show the Fe Kα light curves extracted from the Sgr B2 substructures G0.66-0.13 (Panel 2), G0.56-0.11 (Panel 3), and G0.61+0.00 (Panel 4) outlined in Panel 1. The overall light curve from each substructure is in black, while the light curves of the corresponding 40''-radius features are plotted on the same axes. Substructure G0.66-0.13 was observed to brighten in 2012, but became dim again in 2018. Light curves for the 40''-radius regions (A, B, and C) associated with G0.66-0.13 behave differently over time, with circle A (magenta, farthest from Sgr A\* in the projected plane) brightening only in 2018 while B and C follow the pattern of the parent substructure. Substructure G0.56-0.11 has brightened continuously since 2004, but analysis of 40'' features illustrates that this pattern is not uniform throughout the substructure. Instead, the brightening in 2012 is driven by region marked B (blue) while in 2018 the flux is driven by region A (magenta). Finally, while the light curve for the newly identified structure G0.61+0.00 is consistent with a constant in time, the 40''-radius features again illustrate an evolving morphology within the substructure.

duction within Sgr B2, including via dark matter annihilation.

### 7.1. Implications for the X-ray Reprocessing Scenario

The core and envelope region, previously the brightest part of the cloud, with multiple cores detected (Zhang et al. 2015), is now very faint, as illustrated in Figures 3 and 4. The brightest emission is now restricted to the densest core. One possible explanation is that the major X-ray flare whose reprocessing was previously driving the overall luminosity has now passed through the cloud, and the illumination detected in the 2018 observation is driven by other sources, namely LECR interactions or reprocessing of subdominant X-ray flares. This is consistent with the fact that the luminosity from small bright regions, with their short light crossing times compared to the cloud overall, are expected to have a faster timescale of emission decrease from X-ray reprocessing and thus to better reflect the timescale of the external X-ray source (Terrier et al. 2018).

Multiple scattering of X-rays from the primary external flare would explain the persistent flux in the densest core, even after the flare has passed entirely through the core. Though this signal is anticipated at all wave-

lengths, it is expected to be more prominent in the hard X-ray continuum than in the fluorescent line morphology, as the absorption cross section is larger than the scattering cross section for X-rays below  $\sim 10$  keV (Churazov et al. 2017). The detection of multiple cores above 10 keV against a backdrop of fading emission in the 2013 *NuSTAR* observation (Zhang et al. 2015) suggests that multiple scattering plays an increasingly important role. With spatial resolution up to 79 keV, a future *NuSTAR* observation less severely impacted by stray light would provide clarity on the question of multiple scattering.

In Section 5, we also observed morphological and brightness variation from several X-ray substructures within the diffuse region. G0.56-0.11, which was reported as brightening up in 2012 (Terrier et al. 2018), is even brighter in 2018, with a significant morphologic change. While the 2012 emission is centered on clump B (see Figure 5), the 2018 emission is centered  $\sim 13$  light years (projected distance) away, in clump A. The light curve of clump B gives an upper limit of  $\sim 14$  years for the timescale of the X-ray flare illuminating this region.

Similar light curves to G0.56-0.11 clump B are observed in G0.66-0.13 clumps B and C, suggesting that these two substructures may be illuminated by the same



**Table 3.** The Fe K $\alpha$  flux and brightness from distinct regions of Sgr B2 can probe models of LECR transport into or production within Sgr B2.

Cloud Region	Fe K $\alpha$ flux $10^{-6} \text{ ph cm}^{-2} \text{ s}^{-1}$	Fe K $\alpha$ surface brightness $10^{-7} \text{ ph cm}^{-2} \text{ s}^{-1} \text{ arcmin}^{-2}$	$\chi^2_\nu$ (dof)
Diffuse*	$6.9 \pm 1.9$	$3.2 \pm 0.9$	1.24 (24)
Env. (ellipse) <sup>†</sup>	$2.1 \pm 0.5$	$6.5 \pm 1.4$	1.33 (40)
Env. (0.5' – 2.2') <sup>†</sup>	$12.7 \pm 1.2$	$8.8 \pm 0.8$	1.30 (316)
Core + Env. (0.5')	$1.3 \pm 0.3$	$16.9 \pm 4.1$	1.02 (85)

NOTE—Data are reported based on the 2018 *XMM-Newton* observation of Sgr B2. The region boundaries are in Appendix A (Table 4). Regions are circular or annular, with given angular size in radius, unless otherwise specified. Errors and upper limits indicate 90% confidence. The corresponding spectral fits are in Figure 7.

\*The region selected from the diffuse portion of the cloud is an ellipse, chosen to fall within the diffuse region in both the simplified model and the  $n_H$  observations and to avoid hard point sources. The reported flux is thus the flux from this region, rather than the total flux from the diffuse region. Due to the more limited field of view of MOS1, we calculated flux using MOS2 and pn only for this region.

<sup>†</sup>Because the actual gas distribution in Sgr B2 is more complicated than the simplified model, two distinct sky regions were used to evaluate the envelope flux from Sgr B2, as shown in Figure 6. The annular region, Env. (0.5' – 2.2'), represents the bulk of the envelope in the simplified Sgr B2 model. While the total flux measurement from this region may be useful, Sgr B2 has subdominant cores located within this annulus, and portions of this annular region have a column density more similar to the diffuse region, so the surface brightness should be interpreted with caution. On the other hand, the elliptical envelope region, Env. (ellipse), is a region with typical column density for the Sgr B2 envelope. While the flux for this region does not represent the total flux from the Sgr B2 envelope, the surface brightness is typical of the portions of the cloud with the intermediate column density associated with the envelope.

flaring event, if they are a similar distance from Sgr A\*. Unfortunately, without knowing the line-of-sight position of these structures and their detailed  $n_H$  distributions, we cannot clearly make this claim. Clavel et al. (2013), Chuard et al. (2018), and Terrier et al. (2018) provided evidence for a minimum of two illuminating events propagating through the CMZ, so it is possible that these substructures are illuminated by a different event than the flare providing the bulk of the illumination of the Sgr B2 core and envelope. In the case that these substructures are illuminated by the same event as the core, if we assume Sgr B2 to be at least 50 pc in front of Sgr A\* (following Walls et al. (2016); Yan et al. (2017), and references therein), the substructures could be  $\gtrsim 60$  pc behind Sgr B2, suggesting that they are either not linked to Sgr B2 or that a different event is illuminating these substructures. Future observation by *XMM-Newton* could further constrain the timescales

of these flares based on the future behavior of the “A” clumps from each substructure.

## 7.2. Ambient Low-energy Cosmic Rays

In Table 3, we presented upper limits on any non-time-varying component of the Fe K $\alpha$  emissions from the diffuse, envelope, and core regions of Sgr B2. We excluding cloud regions affected by the variable-luminosity substructures of Section 5 to obtain best upper limits of Fe K $\alpha$  emissions caused by LECR interactions. Here, we discuss these results in the context of ambient LECR populations in the CMZ.

In general, CR transport is modeled as a diffusive process governed by magnetohydrodynamic (MHD) waves, combined with other effects including elastic and inelastic collisions, energy loss via ionization and excitation, and energy loss via synchrotron radiation in the surrounding medium. The details of CR interactions in dense clouds are not clearly established. However, we

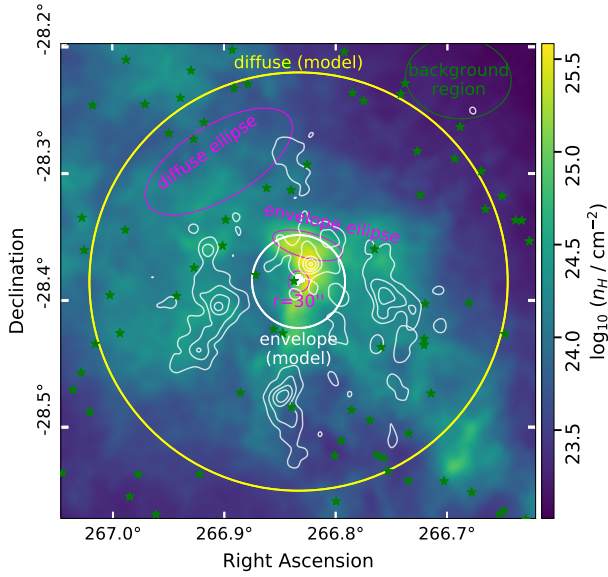


**Figure 6.** The hydrogen column density as measured by Herschel (Molinari et al. 2011) is shown in log scale and illustrates the complexity of the Sgr B2 structure compared to the simple model (yellow,  $9.9'$  diffuse, and white,  $2.2'$  envelope). The regions used in Table 3 are shown as the ellipses (magenta) representing the clean diffuse and envelope regions, and with the  $0.5'$  circle. The background region is also shown (green ellipse), alongside the brightest hard point sources from the Chandra Source Catalog (green stars).

can use the observed rate of hydrogen ionization to trace LECRs in the Galaxy. The low rate of hydrogen ionization within Sgr B2 (van der Tak et al. 2006) compared with the surrounding region (Oka et al. 2005), as well as the low ionization rates in other dense clouds outside the GC compared with diffuse clouds (Indriolo & McCull 2012), provides evidence that LECRs do not freely traverse dense MCs (Dogiel et al. 2015).

Interactions of turbulent neutral gas with ionized hydrogen cause turbulent magnetic fluctuations that impede CR transport in clouds (Dogiel et al. 1987; Istomin & Kiselev 2013). Using a simplified gas distribution of Sgr B2 specifically, Dogiel et al. (2015) calculate that CR propagation in the envelope<sup>1</sup> is best described by diffusion on turbulent magnetic fields. Meanwhile, they assume diffusion is negligible in the diffuse region, where fluctuations are small, such that CR propagation is determined primarily by ionization and excitation. Considering ionization and excitation losses in hydrogen in

the gas model of Sgr B2, protons (electrons) with kinetic energy  $E \lesssim 20$  MeV (1 MeV) are absorbed within the diffuse region. Higher-energy particles can reach the envelope, where they propagate diffusively before being absorbed within  $0.1 - 0.3$  pc (Dogiel et al. 2009a).

In Table 3, we reported the best upper limits on Fe K $\alpha$  emission from the envelope ( $0.5' - 2.2'$ ) region at  $12.7 \pm 1.2 \times 10^{-6}$  ph cm $^{-2}$  s $^{-1}$ . In the LECR proton case, Dogiel et al. (2015) use the relative hydrogen ionization rates in and out of Sgr B2 to find a steady-state solution for CRs in the envelope. They estimate the intensity of Fe K $\alpha$  emission from the Sgr B2 complex as  $I_{6.4} \approx (3 - 5) \frac{Z}{Z_{\odot}} \times 10^{-6}$  ph cm $^{-2}$  s $^{-1}$ , where the range of 3 – 5 depends on the details of the ambient LECR spectrum and the gas distribution of the cloud. Given  $Z/Z_{\odot} = 2$ , the calculation is comparable to the total 2018 Fe K $\alpha$  flux from the envelope region. In other words, the observed Fe K $\alpha$  flux from Sgr B2 in 2018 is comparable to but still larger than that expected from the ambient LECR proton population that could explain the ionization rate in Sgr B2, implying that the 2018 Fe K $\alpha$  emission could be dominated by LECR proton interactions. Future observations by *XMM-Newton* and *NuSTAR* will reveal if the spectra presented here indeed arise from a steady state LECR population or if the light curve will continue to decrease. Should future observations show a decrease to  $\lesssim 50\%$  of the 2018 Fe K $\alpha$  flux, the parameter space for LECR protons in the model by Dogiel et al. (2015) would be strongly constrained.

In the ambient LECR electron case, Dogiel et al. (2015) calculate that a total electron density  $n_e \sim 7.7 \times 10^{-8}$  cm $^{-3}$  is required to explain the observed hydrogen ionization in the Sgr B2 envelope. The X-ray continuum spectrum expected from Bremsstrahlung processes by these electrons is harder than that of an LECR proton or X-ray reprocessing-induced continuum, with a spectral index of  $\sim 1$ . If electrons following the model of Dogiel et al. (2015) were responsible for the full hydrogen ionization rate in Sgr B2, they would produce an excess in the continuum from 20 – 60 keV which should have been observable given the flux levels in 2015. This was not observed (Dogiel et al. 2015), suggesting that an ambient LECR electrons is not the primary source of hydrogen ionization within Sgr B2.

LECR electrons could be produced inside Sgr B2 by interactions of highly relativistic protons. Highly relativistic ambient protons can traverse the cloud to the core, as they are less strongly deflected by magnetic fields than sub-GeV protons and lose less energy through ionization. Inelastic collisions of highly relativistic protons with molecular gas produce secondary charged pions, which decay and ultimately give rise to a popula-

<sup>1</sup> Dogiel et al. (2015) use the term ‘envelope’ for our ‘diffuse region’, and their ‘core’ approximately corresponds to our ‘envelope’. They do not treat the dense star forming cores. For clarity, we have translated their terminology to match this work.

tion of LECR electrons. These electrons are produced within all cloud regions, most abundantly in the core, where the target gas is most dense. Notably, they are not subject to the constraints in Dogiel et al. (2015), which are based on the assumption of ambient external LECR electron diffusion into the cloud.

LECR electrons from ambient relativistic proton interactions could thus be present in the cloud and could contribute to the observed hydrogen ionization rate, despite exclusion of the ambient LECR electron population required to explain the relative ionization inside and outside the cloud. Zhang et al. (2015) excluded LECR electrons as the dominant source of the 2013 emissions based on unphysical spectral fitting results. Considering the Fe K $\alpha$  light curve of the central region presented in Figure 4, the conclusion that the 2013 emission is not dominated by LECR electron interactions is supported by the observed  $\sim 50\%$  Fe K $\alpha$  flux decrease from 2013 to 2018, which indicate that the 2013 emissions were still dominated by time-variable X-ray reprocessing, not LECR electron interactions. The sensitivity of the 2018 observations to LECR electrons and ability to discriminate between proton and electron populations is restricted by the limitations of the *NuSTAR* observation. Thus, we cannot exclude based on these data that LECR electrons produced within Sgr B2 contribute to the bulk of the 2018 X-ray emissions. A future *NuSTAR* observation less severely contaminated by stray light would resolve this ambiguity, as the full *NuSTAR* energy band can identify the hard continuum expected from electron interactions, and the spatial resolution would help distinguish between electrons diffusing into the cloud from the CMZ and electrons produced within the cloud.

### 7.3. Limits on Dark Matter Annihilation

Here we consider the case of LECRs produced within Sgr B2 in the annihilation of dark matter (DM). In this scenario, in contrast to the ambient electrons in Section 7.2, we expect LECR illumination throughout the core and envelope.

Any model of DM annihilating to low-energy electrons or protons would produce a LECR population within GC MCs and thus induce Fe K $\alpha$  fluorescence. The generic DM annihilation rate per unit volume is:

$$\Phi_{DM} = \frac{1}{2} \langle \sigma v \rangle \left( \frac{\rho}{M_{DM}} \right)^2, \quad (1)$$

where the thermally averaged DM annihilation cross section  $\langle \sigma v \rangle$  and DM mass  $M_{DM}$  parametrize the model, and the local DM energy density  $\rho$  is estimated as  $\rho \sim 100 \text{ GeV/cm}^3$  in Sgr B2, given  $\sim 100 \text{ pc}$  distance from the GC (Linden et al. 2011).

To estimate an overly optimistic scenario for observation of DM annihilation to electrons with GC MCs, we assumed that all annihilation energy is transferred to electron kinetic energy. We also assume that all electrons produced in the core and envelope are absorbed within those regions, which is reasonable considering the diffusive dynamics of LECRs within the envelope of Sgr B2 in Section 7.2 and is explicitly treated by Gabici (2013). We considered the  $90''$  sky region surrounding the core of Sgr B2, which represents a spherical volume of  $\sim 165 \text{ pc}^3$  given a distance to Sgr B2 of  $\sim 7.9 \text{ kpc}$ . Comparing our fitted maximum power of LECR electrons in the  $90''$  of Sgr B2,  $P_{LECR_e} < 2.2 \times 10^{40}$ , to the annihilation rate in Eq. (1), we calculated our sensitivity to  $\langle \sigma v \rangle$  in the range of  $3 \times 10^{-22} \text{ cm}^3 \text{ s}^{-1}$  ( $M_{DM} \sim 500 \text{ keV}$ ) to  $6 \times 10^{-19} \text{ cm}^3 \text{ s}^{-1}$  ( $M_{DM} \sim 1 \text{ GeV}$ ).

This best case scenario is several orders of magnitude weaker than both the expected thermal relic annihilation cross section and the existing best limits on  $\langle \sigma v \rangle$  for weakly interacting massive particle (WIMP) DM in this mass range annihilating to all visible products (Leane et al. 2018). Because this calculation assumes that all DM annihilation energy is transferred to the cloud via ionization and excitation by CRs, it is perfectly general to the case of hidden sector DM models as well. As with the WIMP case, existing limits on  $\langle \sigma v \rangle$  for hidden sector DM (Elor et al. 2016) are several orders of magnitude stronger than the best case scenario for limits based on fluorescence in Sgr B2. Thus, for any similar search to succeed in setting leading upper limits on DM annihilation would require a similarly dense cloud with Fe K $\alpha$  emission several orders of magnitude below that presently observe Sgr B2.

## 8. CONCLUSION

Sgr B2 is the most massive molecular cloud in the Central Molecular Zone, and its X-ray features, including a prominent Fe K $\alpha$  line at 6.4 keV and a hard X-ray continuum above 10 keV, have been the subject of observation and discussion for decades. The X-ray features of Sgr B2 provide a window into past energetic activity of Sgr A\*, via X-ray reprocessing in the cloud, and to any sub-GeV cosmic ray populations, via ionization and Bremsstrahlung processes.

In this paper, we have presented the 103ks and 149.2ks observations of Sgr B2 taken jointly in 2018 by the *XMM-Newton* and *NuSTAR* X-ray telescopes, respectively. These data show that the Fe K $\alpha$  emission from the central region of the cloud has decreased by a factor of  $\sim 2$  since the previous *XMM-Newton* (2012) and *NuSTAR* (2013) observations, indicating that the majority of the X-ray flux in observations of Sgr B2 from

2013 and prior originates in X-ray reflection. The 2018 data are consistent with arising either primarily from X-ray reflection or primarily from LECD interactions. Thus, the flux levels presented here represent best upper limits on LECD interactions within different cloud regions. The Fe  $K\alpha$  emission observed from the Sgr B2 envelope is comparable with expectation from the low-energy cosmic proton population that would simultaneously explain hydrogen ionization rates in the model of Dogiel et al. (2015).

Future observations of Sgr B2 by *XMM-Newton* will constrain the Fe  $K\alpha$  light curve from the envelope, core, and the cloud overall, clarifying the origin of the flux observed in 2018 and presented in this paper. If further decrease of the Fe  $K\alpha$  emission from the envelope is observed, the ambient LECD proton model of hydrogen ionization of Dogiel et al. (2015) will begin to be constrained. Meanwhile, further observation of the light curve from the core, especially above 10 keV, where scattering is the dominant photon process, will clarify the multiple scattering picture of the XRN model. With its excellent spatial resolution up to 79 keV, a more clean future *NuSTAR* observation would constrain the hard-continuum light curves from the core and envelope, allowing the cleanest probe of the multiple scattering scenario. Considering the harder X-ray continuum expected from LECD electron interactions relative to LECD proton or XRN processes, future observations from *NuSTAR* would also provide an excellent probe of LECD electrons.

## ACKNOWLEDGMENTS

This research made use of data obtained with *XMM-Newton*, an ESA science mission with instruments and

contribution directly funded by ESA Member States and NASA. This work is supported by XMM-Newton AO Cycle-16 observation grant 80NSSC18K0623. This work also made use of data from *NuSTAR*, a project led by the California Institute of Technology, managed by the Jet Propulsion Laboratory, and funded by NASA. We thank the *NuSTAR* Operations, Software and Calibration teams for support with the execution and analysis of these observations. This research has made use of data obtained through the High Energy Astrophysics Science Archive Research Center Online Service, provided by the NASA/Goddard Space Flight Center.

We gratefully acknowledge Chuck Hailey, Roman Krivonos, Ekaterina Kuznetsova, Kaya Mori, Gabriele Ponti, and Farhad Yusef-Zadeh for enlightening discussions related to Galactic Center cosmic rays and the Sgr B2 region. Special thanks also go to Brandon Roach for sharing his Astropy and data visualization expertise.

F.R. is supported through the National Science Foundation Graduate Research Fellowship Program under Grant No. 1122374. M.C. acknowledges financial support from the French National Research Agency in the framework of the “Investissements d’avenir” program (ANR-15-IDEX-02) and from CNES.

*Facilities:* XMM-Newton, NuSTAR

*Software:* *heasoft* (Nasa High Energy Astrophysics Science Archive Research Center (Heasarc) 2014), *ciao-tools* (Fruscione et al. 2006), *MyTorus* (Yaqoob 2012), *SAOImage ds9* (Joye & Mandel 2003), *Matplotlib* (Hunter 2007), *IPython* (Perez & Granger 2007), and *Astropy* (Astropy Collaboration et al. 2013, 2018)

## APPENDIX

### A. SPECTRAL FITTING OF DIVERSE CLOUD REGIONS

Table 4 lists the sky regions used in the discussion of time variability of substructures discussed in Section 5 as well as those sky regions used in the discussion of LECDs in different portions of the cloud in Section 6. Circular and annular regions centered on the Sgr B2 core are not listed in the table, but all assume the center of the Sgr B2 complex is at RA=17<sup>h</sup>47<sup>m</sup>19.992<sup>s</sup>, Dec=−28°23′07.08″.

The spectral fits used to produce the light curves in Section 5.2 (Figure 5) were made using data extracted from four different *XMM-Newton* observations. To produce the light curve for each substructure, we first selected the observation when that substructure was brightest and performed a spectral fit to the phenomenological model in Section 4.1, freezing  $N_H(f) = 10^{23} \text{ cm}^{-2}$  for consistency between regions. Because the structures are too dim in some epochs to constrain a good fit, we then fixed all model parameters other than the normalizations before fitting the spectra from the other observations. Though constraints based on the large size of Sgr B2, hard point sources, and



**Table 4.** Sky regions used for mapping the time variability of substructures in Section 5 (upper) and setting upper limits on LECR ionization in different cloud regions in Section 6 (lower).

Region Name	R.A.	Dec.	Radius	Minor axis	Major axis	Angle
G0.74-0.10	17 <sup>h</sup> 47 <sup>m</sup> 44.878 <sup>s</sup>	−28°21′22.60″	...	60″	150″	271.212°
G0.75-0.01	17 <sup>h</sup> 47 <sup>m</sup> 22.412 <sup>s</sup>	−28°18′38.91″	40″	...	...	...
G0.66-0.13	17 <sup>h</sup> 47 <sup>m</sup> 41.950 <sup>s</sup>	−28°26′23.15″	...	72″	144″	301.212°
G0.66-0.13 A	17 <sup>h</sup> 47 <sup>m</sup> 39.737 <sup>s</sup>	−28°24′58.48″	40″	...	...	...
G0.66-0.13 B	17 <sup>h</sup> 47 <sup>m</sup> 43.860 <sup>s</sup>	−28°27′08.63″	40″	...	...	...
G0.66-0.13 C	17 <sup>h</sup> 47 <sup>m</sup> 38.365 <sup>s</sup>	−28°25′45.64″	40″	...	...	...
G0.56-0.11	17 <sup>h</sup> 47 <sup>m</sup> 24.879 <sup>s</sup>	−28°30′50.91″	90″	...	...	...
G0.56-0.11 A	17 <sup>h</sup> 47 <sup>m</sup> 27.374 <sup>s</sup>	−28°29′30.58″	40″	...	...	...
G0.56-0.11 B	17 <sup>h</sup> 47 <sup>m</sup> 24.053 <sup>s</sup>	−28°30′52.82″	40″	...	...	...
G0.56-0.11 C	17 <sup>h</sup> 47 <sup>m</sup> 15.249 <sup>s</sup>	−28°31′27.12″	40″	...	...	...
G0.56-0.11 D	17 <sup>h</sup> 47 <sup>m</sup> 18.848 <sup>s</sup>	−28°32′57.32″	40″	...	...	...
G0.61+0.00	17 <sup>h</sup> 47 <sup>m</sup> 03.925 <sup>s</sup>	−28°24′54.11″	...	72″	144″	16.203°
G0.61+0.00 A	17 <sup>h</sup> 47 <sup>m</sup> 04.276 <sup>s</sup>	−28°24′40.44″	40″	...	...	...
G0.61+0.00 B	17 <sup>h</sup> 47 <sup>m</sup> 06.275 <sup>s</sup>	−28°26′44.07″	40″	...	...	...
6′ Region	17 <sup>h</sup> 47 <sup>m</sup> 29.280 <sup>s</sup>	−28°21′57.60″	360″	...	...	...
Diffuse Ellipse	17 <sup>h</sup> 47 <sup>m</sup> 37.123 <sup>s</sup>	−28°17′26.16″	...	104″	236″	301.354°
Envelope Ellipse	17 <sup>h</sup> 47 <sup>m</sup> 18.070 <sup>s</sup>	−28°21′24.22″	...	36″	102″	255°

NOTE—All coordinates are in terms of right ascension (R.A.) and declination (Dec.) using the J2000 system. We assume the Sgr B2 complex is centered on RA=17<sup>h</sup>47<sup>m</sup>19.992<sup>s</sup>, Dec=−28°23′07.08″.

different focused fields of view necessitated use of different sky regions for background subtraction in each observation, cross checks using different background regions in the same observation yielded consistent Fe K $\alpha$  flux measurements.

In Figure 7, we show the spectral fits with the phenomenological model used to produce the light curves in Table 3. Because of the restricted *NuSTAR* field of view, these data are from the 2018 *XMM-Newton* observations only and there is thus no constant factor. The Fe K $\alpha$  flux measurement is based on the spectral fitting with the phenomenological model as in Section 4.1, but we freeze  $N_H(i) = 10^{23} \text{ cm}^{-2}$  and  $Z/Z_\odot = 2$  for a fair comparison between regions, and we froze  $\Gamma = 2$  because the spectral index could not be constrained by the *XMM-Newton* data alone. The surface brightness is calculated using the region area obtained by image analysis (i.e. accounting for missing pixels). The fits to the phenomenological model are satisfactory as evaluated by  $\chi^2_\nu$ .

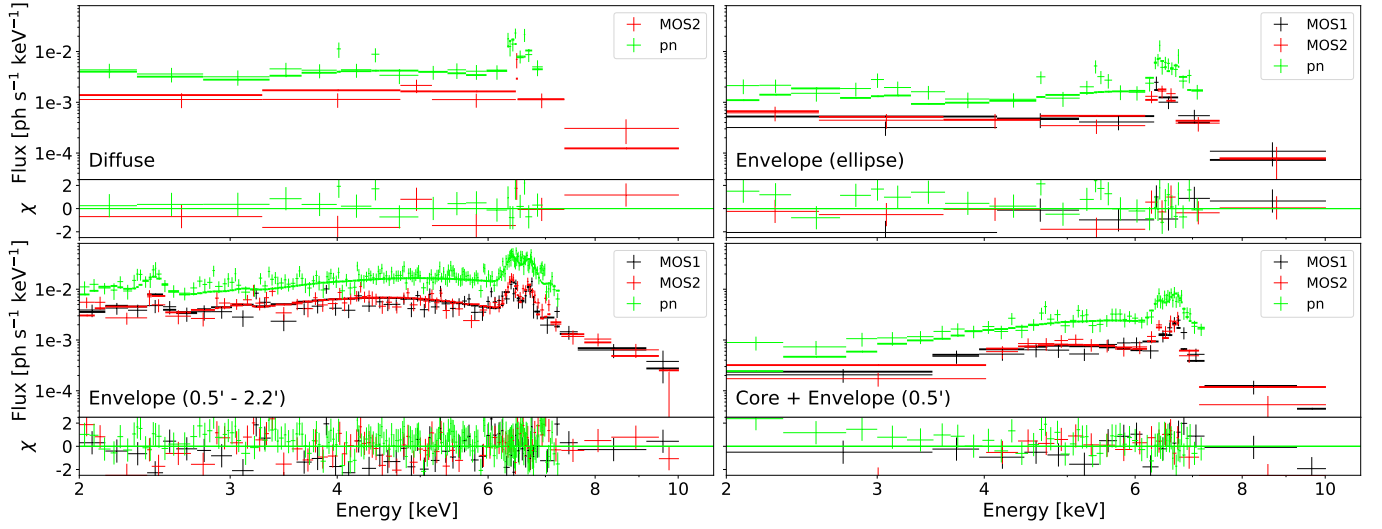


**Figure 7.** The 2018 spectral fits that yield the data presented in Table 3, are shown. Spectra are shown for the Diffuse (upper left), Envelope (ellipse, upper right), Envelope (0.5' - 2.2', lower left), and Core (0.5', lower right) regions (given in Figure 6), fitted with the phenomenological model. The models are fitted simultaneously to data from the *XMM-Newton* MOS1 (black, 2 - 10 keV) MOS2 (red, 2 - 10 keV) and *pn* (green, 2 - 7.8 keV). The Diffuse region is not compatible with the MOS1 field of view. The data are binned with  $3\sigma$  confidence. The best fit is shown in the thick horizontal lines.

## REFERENCES

- Aharonian, F., Akhperjanian, A. G., Bazer-Bachi, A. R., et al. 2006, *Nature*, 439, 695, doi: [10.1038/nature04467](https://doi.org/10.1038/nature04467)
- Albert, A., Alfaro, R., Alvarez, C., et al. 2021, *ApJL*, 907, L30, doi: [10.3847/2041-8213/abd77b](https://doi.org/10.3847/2041-8213/abd77b)
- Anjos, R. C., & Catalani, F. 2020, *PhRvD*, 101, 123015, doi: [10.1103/PhysRevD.101.123015](https://doi.org/10.1103/PhysRevD.101.123015)
- Astropy Collaboration, Robitaille, T. P., Tollerud, E. J., et al. 2013, *A&A*, 558, A33, doi: [10.1051/0004-6361/201322068](https://doi.org/10.1051/0004-6361/201322068)
- Astropy Collaboration, Price-Whelan, A. M., SipHocz, B. M., et al. 2018, *aj*, 156, 123, doi: [10.3847/1538-3881/aabc4f](https://doi.org/10.3847/1538-3881/aabc4f)
- Baganoff, F. K., Maeda, Y., Morris, M., et al. 2003, *ApJ*, 591, 891, doi: [10.1086/375145](https://doi.org/10.1086/375145)
- Barnes, P. J., Muller, E., Indermuhle, B., et al. 2015, *ApJ*, 812, 6, doi: [10.1088/0004-637X/812/1/6](https://doi.org/10.1088/0004-637X/812/1/6)
- Benson, J. M., & Johnston, K. J. 1984, *ApJ*, 277, 181, doi: [10.1086/161680](https://doi.org/10.1086/161680)
- Cesarsky, C. J., & Montmerle, T. 1983, *SSRv*, 36, 173, doi: [10.1007/BF00167503](https://doi.org/10.1007/BF00167503)
- Cheng, K. S., Chernyshov, D. O., Dogiel, V. A., et al. 2012, *ApJ*, 746, 116, doi: [10.1088/0004-637X/746/2/116](https://doi.org/10.1088/0004-637X/746/2/116)
- Chuard, D., Terrier, R., Goldwurm, A., et al. 2018, *A&A*, 610, A34, doi: [10.1051/0004-6361/201731864](https://doi.org/10.1051/0004-6361/201731864)
- Churazov, E., Khabibullin, I., Ponti, G., & Sunyaev, R. 2017, *MNRAS*, 468, 165, doi: [10.1093/mnras/stx443](https://doi.org/10.1093/mnras/stx443)
- Clavel, M., Terrier, R., Goldwurm, A., et al. 2013, *A&A*, 558, A32, doi: [10.1051/0004-6361/201321667](https://doi.org/10.1051/0004-6361/201321667)
- de Vicente, P., Martin-Pintado, J., & Wilson, T. L. 1997, *A&A*, 320, 957
- Dobler, G., Finkbeiner, D. P., Cholis, I., Slatyer, T., & Weiner, N. 2010, *ApJ*, 717, 825, doi: [10.1088/0004-637X/717/2/825](https://doi.org/10.1088/0004-637X/717/2/825)
- Dogiel, V., Cheng, K.-S., Chernyshov, D., et al. 2009a, *PASJ*, 61, 901, doi: [10.1093/pasj/61.4.901](https://doi.org/10.1093/pasj/61.4.901)
- Dogiel, V. A., Gurevich, A. V., Istomin, I. N., & Zybin, K. P. 1987, *MNRAS*, 228, 843, doi: [10.1093/mnras/228.4.843](https://doi.org/10.1093/mnras/228.4.843)
- Dogiel, V. A., Chernyshov, D. O., Yuasa, T., et al. 2009b, *PASJ*, 61, 1099, doi: [10.1093/pasj/61.5.1099](https://doi.org/10.1093/pasj/61.5.1099)
- Dogiel, V. A., Chernyshov, D. O., Kiselev, A. M., et al. 2015, *ApJ*, 809, 48, doi: [10.1088/0004-637X/809/1/48](https://doi.org/10.1088/0004-637X/809/1/48)
- Elor, G., Rodd, N. L., Slatyer, T. R., & Xue, W. 2016, *JCAP*, 2016, 024, doi: [10.1088/1475-7516/2016/06/024](https://doi.org/10.1088/1475-7516/2016/06/024)
- Etzaluze, M., Goicoechea, J. R., Cernicharo, J., et al. 2013, *A&A*, 556, A137, doi: [10.1051/0004-6361/201321258](https://doi.org/10.1051/0004-6361/201321258)
- Evans, I. N., Allen, C. E., Anderson, C. S., et al. 2018, in *American Astronomical Society Meeting Abstracts*, Vol. 231, American Astronomical Society Meeting Abstracts #231, 238.01
- Evoli, C., Gaggero, D., Vittino, A., et al. 2017, *JCAP*, 2017, 015, doi: [10.1088/1475-7516/2017/02/015](https://doi.org/10.1088/1475-7516/2017/02/015)
- Fruscione, A., McDowell, J. C., Allen, G. E., et al. 2006, in *Society of Photo-Optical Instrumentation Engineers (SPIE) Conference Series*, Vol. 6270, Society of Photo-Optical Instrumentation Engineers (SPIE) Conference Series, ed. D. R. Silva & R. E. Doxsey, 62701V, doi: [10.1117/12.671760](https://doi.org/10.1117/12.671760)
- Gabici, S. 2013, in *Cosmic Rays in Star-Forming Environments*, ed. D. F. Torres & O. Reimer, Vol. 34, 221, doi: [10.1007/978-3-642-35410-6\\_16](https://doi.org/10.1007/978-3-642-35410-6_16)
- Ghez, A. M., Salim, S., Weinberg, N. N., et al. 2008, *ApJ*, 689, 1044, doi: [10.1086/592738](https://doi.org/10.1086/592738)
- Guépin, C., Rinchuso, L., Kotera, K., et al. 2018, *JCAP*, 2018, 042, doi: [10.1088/1475-7516/2018/07/042](https://doi.org/10.1088/1475-7516/2018/07/042)
- Harrison, F. A., Craig, W. W., Christensen, F. E., et al. 2013, *ApJ*, 770, 103, doi: [10.1088/0004-637X/770/2/103](https://doi.org/10.1088/0004-637X/770/2/103)
- HESS Collaboration, Abramowski, A., Aharonian, F., et al. 2016, *Nature*, 531, 476, doi: [10.1038/nature17147](https://doi.org/10.1038/nature17147)
- Heywood, I., Camilo, F., Cotton, W. D., et al. 2019, *Nature*, 573, 235, doi: [10.1038/s41586-019-1532-5](https://doi.org/10.1038/s41586-019-1532-5)
- Hillas, A. M. 2005, *Journal of Physics G Nuclear Physics*, 31, R95, doi: [10.1088/0954-3899/31/5/R02](https://doi.org/10.1088/0954-3899/31/5/R02)
- Hunter, J. D. 2007, *Computing in Science Engineering*, 9, 90, doi: [10.1109/MCSE.2007.55](https://doi.org/10.1109/MCSE.2007.55)
- Indriolo, N., & McCall, B. J. 2012, *ApJ*, 745, 91, doi: [10.1088/0004-637X/745/1/91](https://doi.org/10.1088/0004-637X/745/1/91)
- Inui, T., Koyama, K., Matsumoto, H., & Tsuru, T. G. 2009, *PASJ*, 61, S241, doi: [10.1093/pasj/61.sp1.S241](https://doi.org/10.1093/pasj/61.sp1.S241)
- Istomin, Y. N., & Kiselev, A. 2013, *MNRAS*, 436, 2774, doi: [10.1093/mnras/stt1785](https://doi.org/10.1093/mnras/stt1785)
- Jaupart, É., Parizot, É., & Allard, D. 2018, *A&A*, 619, A12, doi: [10.1051/0004-6361/201833683](https://doi.org/10.1051/0004-6361/201833683)
- Jones, P. A., Burton, M. G., Tothill, N. F. H., & Cunningham, M. R. 2011, *Monthly Notices of the Royal Astronomical Society*, 411, 2293, doi: [10.1111/j.1365-2966.2010.17849.x](https://doi.org/10.1111/j.1365-2966.2010.17849.x)
- Jouvin, L., Lemi re, A., & Terrier, R. 2020, *A&A*, 644, A113, doi: [10.1051/0004-6361/202039069](https://doi.org/10.1051/0004-6361/202039069)
- Joye, W. A., & Mandel, E. 2003, in *Astronomical Society of the Pacific Conference Series*, Vol. 295, *Astronomical Data Analysis Software and Systems XII*, ed. H. E. Payne, R. I. Jedrzejewski, & R. N. Hook, 489
- Kataoka, J., Sofue, Y., Inoue, Y., et al. 2018, *Galaxies*, 6, 27, doi: [10.3390/galaxies6010027](https://doi.org/10.3390/galaxies6010027)

- Koyama, K., Maeda, Y., Sonobe, T., et al. 1996, PASJ, 48, 249, doi: [10.1093/pasj/48.2.249](https://doi.org/10.1093/pasj/48.2.249)
- Koyama, K., Inui, T., Hyodo, Y., et al. 2007, PASJ, 59, 221, doi: [10.1093/pasj/59.sp1.S221](https://doi.org/10.1093/pasj/59.sp1.S221)
- Krivonos, R. A., Tomsick, J. A., Bauer, F. E., et al. 2014, ApJ, 781, 107, doi: [10.1088/0004-637X/781/2/107](https://doi.org/10.1088/0004-637X/781/2/107)
- Kuznetsova, E., Krivonos, R., Lutovinov, A., & Clavel, M. 2021, submitted to MNRAS
- LaRosa, T. N., Kassim, N. E., Lazio, T. J. W., & Hyman, S. D. 2000, AJ, 119, 207, doi: [10.1086/301168](https://doi.org/10.1086/301168)
- Le Petit, F., Ruaud, M., Bron, E., et al. 2016, A&A, 585, A105, doi: [10.1051/0004-6361/201526658](https://doi.org/10.1051/0004-6361/201526658)
- Leane, R. K., Slatyer, T. R., Beacom, J. F., & Ng, K. C. Y. 2018, PhRvD, 98, 023016, doi: [10.1103/PhysRevD.98.023016](https://doi.org/10.1103/PhysRevD.98.023016)
- Linden, T., Hooper, D., & Yusef-Zadeh, F. 2011, ApJ, 741, 95, doi: [10.1088/0004-637X/741/2/95](https://doi.org/10.1088/0004-637X/741/2/95)
- Lis, D. C., & Goldsmith, P. F. 1990, ApJ, 356, 195, doi: [10.1086/168830](https://doi.org/10.1086/168830)
- McClure-Griffiths, N. M., Green, J. A., Hill, A. S., et al. 2013, ApJL, 770, L4, doi: [10.1088/2041-8205/770/1/L4](https://doi.org/10.1088/2041-8205/770/1/L4)
- Medina-Torrejón, T. E., de Gouveia Dal Pino, E. M., Kadowaki, L. H. S., et al. 2021, ApJ, 908, 193, doi: [10.3847/1538-4357/ab0d82](https://doi.org/10.3847/1538-4357/ab0d82)
- Molinari, S., Bally, J., Noriega-Crespo, A., et al. 2011, ApJL, 735, L33, doi: [10.1088/2041-8205/735/2/L33](https://doi.org/10.1088/2041-8205/735/2/L33)
- Morlino, G., & Gabici, S. 2015, MNRAS, 451, L100, doi: [10.1093/mnras/slv074](https://doi.org/10.1093/mnras/slv074)
- Morris, M., & Serabyn, E. 1996, ARA&A, 34, 645, doi: [10.1146/annurev.astro.34.1.645](https://doi.org/10.1146/annurev.astro.34.1.645)
- Muno, M. P., Baganoff, F. K., Bautz, M. W., et al. 2004, ApJ, 613, 326, doi: [10.1086/422865](https://doi.org/10.1086/422865)
- Murakami, H., Koyama, K., & Maeda, Y. 2001, ApJ, 558, 687, doi: [10.1086/322282](https://doi.org/10.1086/322282)
- Murphy, K. D., & Yaqoob, T. 2009, MNRAS, 397, 1549, doi: [10.1111/j.1365-2966.2009.15025.x](https://doi.org/10.1111/j.1365-2966.2009.15025.x)
- Nakashima, S., Koyama, K., Wang, Q. D., & Enokiya, R. 2019, ApJ, 875, 32, doi: [10.3847/1538-4357/ab0d82](https://doi.org/10.3847/1538-4357/ab0d82)
- Nasa High Energy Astrophysics Science Archive Research Center (Heasarc). 2014, HEASoft: Unified Release of FTOOLS and XANADU. <http://ascl.net/1408.004>
- Nobukawa, M., Ryu, S. G., Tsuru, T. G., & Koyama, K. 2011, ApJL, 739, L52, doi: [10.1088/2041-8205/739/2/L52](https://doi.org/10.1088/2041-8205/739/2/L52)
- Oka, T., Geballe, T. R., Goto, M., et al. 2019, ApJ, 883, 54, doi: [10.3847/1538-4357/ab3647](https://doi.org/10.3847/1538-4357/ab3647)
- Oka, T., Geballe, T. R., Goto, M., Usuda, T., & McCall, B. J. 2005, ApJ, 632, 882, doi: [10.1086/432679](https://doi.org/10.1086/432679)
- Owen, E. R., On, A. Y. L., Lai, S.-P., & Wu, K. 2021, ApJ, 913, 52, doi: [10.3847/1538-4357/abee1a](https://doi.org/10.3847/1538-4357/abee1a)
- Perez, F., & Granger, B. E. 2007, Computing in Science Engineering, 9, 21, doi: [10.1109/MCSE.2007.53](https://doi.org/10.1109/MCSE.2007.53)
- Ponti, G., Morris, M. R., Churazov, E., Heywood, I., & Fender, R. P. 2021, A&A, 646, A66, doi: [10.1051/0004-6361/202039636](https://doi.org/10.1051/0004-6361/202039636)
- Ponti, G., Morris, M. R., Terrier, R., et al. 2015, MNRAS, 453, 172, doi: [10.1093/mnras/stv1331](https://doi.org/10.1093/mnras/stv1331)
- Ponti, G., Hofmann, F., Churazov, E., et al. 2019, Nature, 567, 347, doi: [10.1038/s41586-019-1009-6](https://doi.org/10.1038/s41586-019-1009-6)
- Predehl, P., Sunyaev, R. A., Becker, W., et al. 2020, Nature, 588, 227, doi: [10.1038/s41586-020-2979-0](https://doi.org/10.1038/s41586-020-2979-0)
- Ptuskin, V. S., & Khazan, Y. M. 1981, AZh, 58, 959
- Reid, M. J., Menten, K. M., Zheng, X. W., et al. 2009, ApJ, 700, 137, doi: [10.1088/0004-637X/700/1/137](https://doi.org/10.1088/0004-637X/700/1/137)
- Revnivtsev, M. G., Churazov, E. M., Sazonov, S. Y., et al. 2004, A&A, 425, L49, doi: [10.1051/0004-6361:200400064](https://doi.org/10.1051/0004-6361:200400064)
- Sato, F., Hasegawa, T., Whiteoak, J. B., & Miyawaki, R. 2000, ApJ, 535, 857, doi: [10.1086/308856](https://doi.org/10.1086/308856)
- Snowden, S. L., Mushotzky, R. F., Kuntz, K. D., & Davis, D. S. 2008, A&A, 478, 615, doi: [10.1051/0004-6361:20077930](https://doi.org/10.1051/0004-6361:20077930)
- Sofue, Y., & Kataoka, J. 2021, MNRAS, 506, 2170, doi: [10.1093/mnras/stab1857](https://doi.org/10.1093/mnras/stab1857)
- Strong, A. W., Moskalenko, I. V., & Ptuskin, V. S. 2007, Annual Review of Nuclear and Particle Science, 57, 285, doi: [10.1146/annurev.nucl.57.090506.123011](https://doi.org/10.1146/annurev.nucl.57.090506.123011)
- Strüder, L., Briel, U., Dennerl, K., et al. 2001, A&A, 365, L18, doi: [10.1051/0004-6361:20000066](https://doi.org/10.1051/0004-6361:20000066)
- Su, M., Slatyer, T. R., & Finkbeiner, D. P. 2010, ApJ, 724, 1044, doi: [10.1088/0004-637X/724/2/1044](https://doi.org/10.1088/0004-637X/724/2/1044)
- Sunyaev, R., & Churazov, E. 1998, MNRAS, 297, 1279, doi: [10.1046/j.1365-8711.1998.01684.x](https://doi.org/10.1046/j.1365-8711.1998.01684.x)
- Sunyaev, R. A., Markevitch, M., & Pavlinsky, M. 1993, ApJ, 407, 606, doi: [10.1086/172542](https://doi.org/10.1086/172542)
- Tatischeff, V., Decourchelle, A., & Maurin, G. 2012, A&A, 546, A88, doi: [10.1051/0004-6361/201219016](https://doi.org/10.1051/0004-6361/201219016)
- Terrier, R., Clavel, M., Soldi, S., et al. 2018, A&A, 612, A102, doi: [10.1051/0004-6361/201730837](https://doi.org/10.1051/0004-6361/201730837)
- Terrier, R., Ponti, G., Bélanger, G., et al. 2010, ApJ, 719, 143, doi: [10.1088/0004-637X/719/1/143](https://doi.org/10.1088/0004-637X/719/1/143)
- Turner, M. J. L., Abbey, A., Arnaud, M., et al. 2001, A&A, 365, L27, doi: [10.1051/0004-6361:20000087](https://doi.org/10.1051/0004-6361:20000087)
- Valinia, A., Tatischeff, V., Arnaud, K., Ebisawa, K., & Ramaty, R. 2000, ApJ, 543, 733, doi: [10.1086/317133](https://doi.org/10.1086/317133)
- van der Tak, F. F. S., Belloche, A., Schilke, P., et al. 2006, A&A, 454, L99, doi: [10.1051/0004-6361:20065289](https://doi.org/10.1051/0004-6361:20065289)
- Walls, M., Chernyakova, M., Terrier, R., & Goldwurm, A. 2016, MNRAS, 463, 2893, doi: [10.1093/mnras/stw2181](https://doi.org/10.1093/mnras/stw2181)



- Yan, Q.-Z., Walsh, A. J., Dawson, J. R., et al. 2017, Monthly Notices of the Royal Astronomical Society, 471, 2523, doi: [10.1093/mnras/stx1724](https://doi.org/10.1093/mnras/stx1724)
- Yang, H. Y., Ruszkowski, M., & Zweibel, E. 2018, Galaxies, 6, 29, doi: [10.3390/galaxies6010029](https://doi.org/10.3390/galaxies6010029)
- Yaqoob, T. 2012, MNRAS, 423, 3360, doi: [10.1111/j.1365-2966.2012.21129.x](https://doi.org/10.1111/j.1365-2966.2012.21129.x)
- Yusef-Zadeh, F., Munro, M., Wardle, M., & Lis, D. C. 2007, ApJ, 656, 847, doi: [10.1086/510663](https://doi.org/10.1086/510663)
- Yusef-Zadeh, F., & Wardle, M. 2019, MNRAS, 490, L1, doi: [10.1093/mnrasl/slz134](https://doi.org/10.1093/mnrasl/slz134)
- Yusef-Zadeh, F., Hewitt, J. W., Wardle, M., et al. 2013, ApJ, 762, 33, doi: [10.1088/0004-637X/762/1/33](https://doi.org/10.1088/0004-637X/762/1/33)
- Zhang, R., & Guo, F. 2020, ApJ, 894, 117, doi: [10.3847/1538-4357/ab8bd0](https://doi.org/10.3847/1538-4357/ab8bd0)
- Zhang, S., Hailey, C. J., Baganoff, F. K., et al. 2014, ApJ, 784, 6, doi: [10.1088/0004-637X/784/1/6](https://doi.org/10.1088/0004-637X/784/1/6)
- Zhang, S., Hailey, C. J., Mori, K., et al. 2015, ApJ, 815, 132, doi: [10.1088/0004-637X/815/2/132](https://doi.org/10.1088/0004-637X/815/2/132)
- Zhang, S., Zhu, Z., Li, H., et al. 2020, ApJ, 893, 3, doi: [10.3847/1538-4357/ab7dc1](https://doi.org/10.3847/1538-4357/ab7dc1)